Thesis for the degree of Doctor of Philosophy

Colloidal synthesis of metal nanoparticles

Mechanistic studies and development of flow synthesis routes

ANNA PEKKARI

CHALMERS

Department of Chemistry and Chemical Engineering
CHALMERS UNIVERSITY OF TECHNOLOGY
Gothenburg, Sweden 2020

Colloidal synthesis of metal nanoparticles
Mechanistic studies and development of flow synthesis routes
Anna Pekkari

ISBN 978-91-7905-392-5

Doktorsavhandlingar vid Chalmers tekniska högskola,
Ny serie nr. 4859
ISSN 0346-718X

Department of Chemistry and Chemical Engineering
Chalmers University of Technology
SE-412 96 Gothenburg
Sweden
Telephone +46 (0)31 772 1000

Cover:
Illustration of the synthesis of Au nanoparticles in a continuous segmented flow reactor

Typeset in LaTeX
Printed by Chalmers Reproservice
Gothenburg, Sweden 2020

Colloidal synthesis of metal nanoparticles
Mechanistic studies and development of flow synthesis routes

Anna Pekkari
Department of Chemistry and Chemical Engineering
Chalmers University of Technology

Abstract

Metal nanoparticles (NPs) are central in a wide range of industrial areas including catalytic and biomedical applications. Due to their interesting physical properties, the demand of these precious materials is steadily increasing, which has created a need for the development of effective and high-performing NPs. Because the properties are closely correlated to NP size, shape, and crystal structure, the development of controlled synthesis of metal NPs has emerged. However, the challenge of understanding how reaction parameters influence the outcome of the synthesis currently limits the production of precisely designed metal NPs. Additionally, low reproducibility and control during scale-up has often restricted the production to small scale which limits the use in industrial applications.
The studies presented in this thesis focus on the controlled synthesis of uniform metal NPs using solution-based colloidal methods. Firstly, the multiple roles of the NP stabilizers were investigated. In the synthesis of Cu NPs, alkanethiol stabilizers only provided temporary stabilization of the Cu NPs and decomposed under heating in inert atmosphere, forming Cu_2S NPs. In another study, uniform Pd NPs stabilized with a binary surfactant combination were synthesized without using traditional reductants. The fatty acid stabilizer contributed to the reduction of Pd-precursors, and the reduction kinetics follow a pseudo-first order kinetics. The specific stabilizers investigated influence reduction kinetics, NP sizes and shapes. Secondly, to address scale-up challenges in NP synthesis, the development of flow synthesis routes were explored. Uniform Pd nanocubes (NCs) and PdPt core-shell NPs were produced in a single-phase flow reactor, and a segmented flow reactor was developed to produce uniform Au NPs. The flow production was scaled-up, and the uniformity of Au NPs was confirmed by inline optical spectroscopy quality control. Catalytic evaluation of the function of PdPt core-shell NPs in a model NO_2 reduction reaction showed improved catalytic activity, selectivity and temperature stability compared to Pd NCs.

Keywords: copper, palladium, platinum, gold, nanoparticles, colloidal synthesis, stabilizers, reduction kinetics, flow chemistry, core-shell, nanocube, segmented flow, inline quality control, NO_2 reduction

List of Publications

This thesis is based on the following appended papers:

I. Synthesis of Cu nanoparticles: stability and conversion into Cu_2S nanoparticles by decomposition of alkanethiolate
Christian Rohner, Anna Pekkari, Hanna Härelind and Kasper Moth-Poulsen
Published, Langmuir, 2017, 33, 13272-13276

II. Synthesis of highly monodisperse Pd nanoparticles using a binary surfactant combination with sodium oleate as reductant
Anna Pekkari, Xin Wen, Jessica Orrego-Hernández, Robson Rosa da Silva, Eva Olsson, Hanna Härelind, and Kasper Moth-Poulsen
Submitted

III. Continuous microfluidic synthesis of Pd nanocubes and PdPt core-shell nanoparticles and their catalysis of NO_2reduction
Anna Pekkari, Zafer Say, Arturo Susarrey-Arce, Christoph Langhammer, Hanna Härelind, Victor Sebastian and Kasper Moth-Poulsen
Published, ACS Applied Materials and interfaces, 2019, 11, 36196-36204

IV. Continuous hydrothermal flow synthesis of monodisperse citrate-capped Au nanoparticles: a non-fouling efficient route by using paraffin-water segmented system and inline liquid-liquid phase separation
Anna Pekkari, Orlane Nicolardot, Robson Rosa da Silva, Xin Wen, Jessica Orrego-Hernández, Hanna Härelind, and Kasper Moth-Poulsen
Submitted

Additional publications not included in this thesis:

Guided selective deposition of nanoparticles by tuning of the surface potential
J. Eklöf, A. Stolaś, M. Herzberg, A. Pekkari, B. Tebikachew, T. Gschneidtner, S. Lara-Avila, T. Hassenkam and K. Moth-Poulsen
Published, Europhysics Letters, 2017, 1, 18004

Microwave-heated γ-Alumina Applied to the Chemoselective Reduction of Aldehydes to Alcohols
B. Dhokale, A. Susarrey-Arce, A. Pekkari, A. Runemark, K. Moth-Poulsen, C. Langhammer, H. Härelind, M. Busch, M. Vandichel, and H. Sundén
Accepted ChemCatChem, (2020)

My Contributions to the Publications

Paper I
Second author. I conducted synthesis experiments, TEM and UV-Vis analysis. XRD and electron diffraction was performed by Christian Rohner. Part of the writing and proof reading.

Paper II
Main author. I conducted all the synthesis experiments, sample preparation, UV-Vis and FTIR analysis. HRTEM and electron diffraction was performed by Xin Wen. NMR measurements was performed by Jessica Orrego-Hernández. I wrote the first draft and was responsible for writing the manuscript.

Paper III
Main author. I conducted all the synthesis experiments, SEM analysis and performed data analysis and interpreted the results with my co-authors. TEM, HRTEM and EDX analysis was performed by Victor Sebastian. The catalytic evaluation was performed by Zafer Say. I wrote the first draft and was responsible for writing the manuscript.

Paper IV
Main author, shared equally with Orlane Nicolardot. I conducted synthesis experiments, UV-Vis, Zeta potential measurements and TEM analysis. HRTEM was performed by Xin Wen. I wrote the first draft and was responsible for writing the manuscript.

Contents

1 Introduction **1**
1.1 Scope of thesis 2

2 Shaped metal nanoparticles **3**
2.1 Colloidal synthesis 3
2.1.1 Shape-control 4
2.1.2 Bimetallic nanoparticles 6
2.2 Flow synthesis of nanoparticles 7
2.3 Pd and Pt nanoparticles in catalysis 9

3 Synthesis and characterization methods **11**
3.1 Colloidal synthesis and kinetic evaluation 11
3.1.1 Synthesis of Cu and Cu_2S nanoparticles 11
3.1.2 Synthesis and reduction kinetics of Pd nanoparticles 12
3.2 Flow synthesis of nanoparticles 13
3.2.1 Single-phase flow synthesis of Pd nanocubes and PdPt nanoparticles 13
3.2.2 Continuous segmented flow synthesis of Au nanoparticles 14
3.3 Characterization of nanoparticles 15
3.3.1 Transmission electron microscopy 15
3.3.2 Scanning electron microscopy 16
3.3.3 Ultraviolet-visible spectroscopy 16
3.3.4 Powder x-ray diffraction 16
3.3.5 Microwave plasma atomic emission spectroscopy 17
3.3.6 Fourier transform infrared spectroscopy 17
3.3.7 Nuclear magnetic resonance 17
3.3.8 Zeta potential 18

3.3.9 Catalytic evaluation 18

4 Results and discussion **19**
4.1 Stabilizer effects and reduction mechanisms for colloidal nanoparticles . 19
4.1.1 Multiple roles of stabilizers 19
4.1.2 Evaluation of reduction kinetics 24
4.2 Flow synthesis of colloidal nanoparticles 27
4.2.1 Development of a single-phase flow synthesis 27
4.2.2 Development of an automated segmented flow synthesis 29
4.2.3 Flow synthesis optimization - effect of temperature 31
4.2.4 Scale-up of flow production 33
4.2.5 Catalytic evaluation of Pd and PdPt nanoparticles 37

5 Conclusions and Reflections **39**
5.1 Contribution to the field of nanoparticle synthesis 40
5.2 Reflections on future development of nanoparticle synthesis 40

Acknowledgements **43**

Bibliography **45**

Chapter 1

Introduction

The development of metal nanoparticles (NPs) (including Cu, Au, Pd and Pt) has gained immense interest in the recent years due to their interesting and unique physical properties, and has led to their applications in a range of areas including catalysis[1, 2], fuel cells[3], and biomedical applications[4,5]. The steadily increasing demand of these precious materials has created a need for the development of effective and high-performing NPs. Since the properties of the metal NPs are closely related to the size, shape and composition, the development of synthesis methods with a high degree of control over these properties have emerged[6, 7]. By replacing NPs with heterogeneous morphology with precisely designed NPs with higher performance, the material loading in the defined application can be reduced and the cost lowered, and thus a more sustainable use of these rare metals can be achieved[8]. Among the wide range of existing NP synthesis methods, solution-based colloidal methods have created a range of defined shaped NPs and benefit from its simplicity, reproducibility and high precision in controlling NP properties[9–11]. However, the lack of understanding of how different reaction parameters influence the outcome of the synthesis is currently a challenge in the development of precisely structured metal NPs[12]. Moreover, for controlled metal NPs to target industrial applications the production has to be scaled-up to the kilogram-scale[8, 13]. The batch reactors traditionally used for the synthesis of controlled metal NPs are often limited to small scale due to inefficient mixing and heat transfer during production scale-up which has led to poor reproducibility between batches[8, 14]. An approach to address these challenges is to synthesize NPs in flow reactors. Reagents are continuously infused in micro- or millimeter sized channels, which provide fast mass transfer and heating with high control over reaction parameters[15–18]. The synthesis can be scaled up by flow reactor parallelization[19], increase of flow channel dimensions[13, 20], and extended operation times and NP quality can be continuously monitored by inline quality control[21].

1.1 Scope of thesis

The primary objective of the work presented in this thesis was to develop an increased understanding of what factors control the synthesis of uniform metal NPs using solution-based colloidal methods. The first part of this thesis focuses on understanding synthesis mechanisms and the influence on NP properties. In **Paper I**, thiol-stabilized Cu NPs were synthesized and the decomposition route of the thiol stabilizer and the formation of Cu_2S NPs was studied. In **Paper II**, Pd NPs stabilized with a binary surfactant combination were synthesized without traditional reducing agents, and the reduction mechanisms and kinetics were studied. The second part of the thesis involves the development of continuous flow synthesis routes to address scale-up challenges in NP synthesis. In **Paper III** a flow synthesis is designed for the synthesis of Pd nanocubes (NCs) and PdPt core-shell NPs, and process scalability explored. Furthermore, the catalytic performance of the Pd and PdPt NPs was evaluated in a model NO_2 reduction reaction. **Paper IV** focuses on exploring the development of an automated segmented flow synthesis to produce uniform citrate-capped Au NPs in large scale. The Au NP reaction phase is separated by liquid-liquid phase separation, and product quality monitored inline by optical spectroscopy.

Chapter 2

Shaped metal nanoparticles

2.1 Colloidal synthesis

Precisely shape and size-controlled metal NPs have mainly been synthesized using solution-based colloidal methods, which have successfully explored a wide range of metals and structures[9–11]. In the general procedure, a metal salt precursor is reduced in solution by a reductant, which supplies the metal with electrons. A variety of reductants have been employed in the synthesis of NPs, such as ascorbic acid, sodium borohydride, trisodium citrate and alcohols. Apart from donating electrons, the reductant can sometimes have several roles such as capping agent, colloidal stabilizer or solvent. Careful choice of reductant is essential since its physicochemical properties influence the reduction kinetics and subsequent outcome of the NP synthesis[22]. Other components normally present in the colloidal method are capping agents or stabilizers that provide colloidal stabilization and prevent aggregation by adsorption onto the NP surface. Commonly employed stabilizers in NP synthesis include surfactants, thiols, polymers, and fatty acids[23].

LaMer theory [24] is the predominant theory that explains NP formation in solution, which is divided into two distinct stages; nucleation and growth (Figure 2.1). Initially (I), the metal precursor is rapidly reduced, and when the metal atom concentration reaches a critical concentration (II), the burst nucleation point, plenty of metal nuclei form. Particles continue to grow by coalescence of the nuclei followed by slow growth by diffusion (III). A rapid nucleation that creates multiple particle seeds is considered crucial for the production of uniform NPs[25]. Uniform or monodisperse NPs are defined as having a narrow size distribution with a size deviation below 10 % [26]. A precise control of size and shape of NPs can be achieved by fine tuning the nucleation and growth steps. This can be attained either by thermodynamic (reaction temperature, reduction potentials) or kinetic control (reagent concentration, reaction

rate, solubility)[25, 27]. Nonetheless, to understand the effect of each parameter and how it influences the outcome of the synthesis is challenging. Several models have tried to explain NP growth and kinetics[28], but additional knowledge is needed to fully understand reduction mechanisms involved in NP synthesis[12, 29].

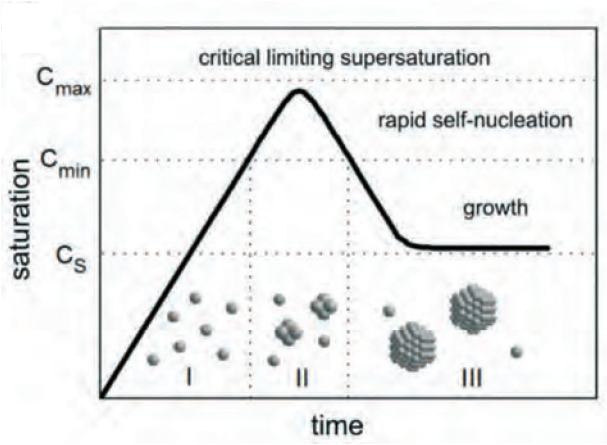

Figure 2.1: The principle of NP nucleation and growth according to LaMer theory. The curve shows the metal precursor concentration as a function of time. [29] - Published by The Royal Society of Chemistry.

2.1.1 Shape-control

In the synthesis of metal NPs, the shape can be directed by thermodynamics and kinetics [25, 27, 30, 31], presented in the energy diagram in Figure 2.2. The lowest free energy of the NP system is the product formed under thermodynamic control. A kinetic product which has a higher energy can form at a local energy minimum. The driving force for any kinetic product is to convert to the thermodynamic state, where a certain amount of energy is required to cross the activation energy barrier. Depending on the size of the energy barrier and thermal energy present in the system, the kinetic product can be stable for different periods of time [27, 30].

For a crystalline material, surface area is not the only factor determining the surface free energy. The type of crystal structure possesses different surface free energies depending on their atom arrangements. The metals applied in this thesis work (Cu, Au, Pd, Pt) are face-centered cubic (fcc) metals for which three of the low-index crystal planes are (111), (100) and (110) (Figure 2.3a). The more dangling bonds a surface contains, the more unstable it is and the higher surface free energy it has. The number of dangling bonds increases for (111), (100) and (110) crystal planes from 3,4 to 6, and consequently the surface free energies follow the same pattern [27]. The Wulff polyhedron is the thermodynamically most favorable shape, having the lowest surface energy [31]. It consists of (111) and (100) facets and is referred to as polycrystalline.

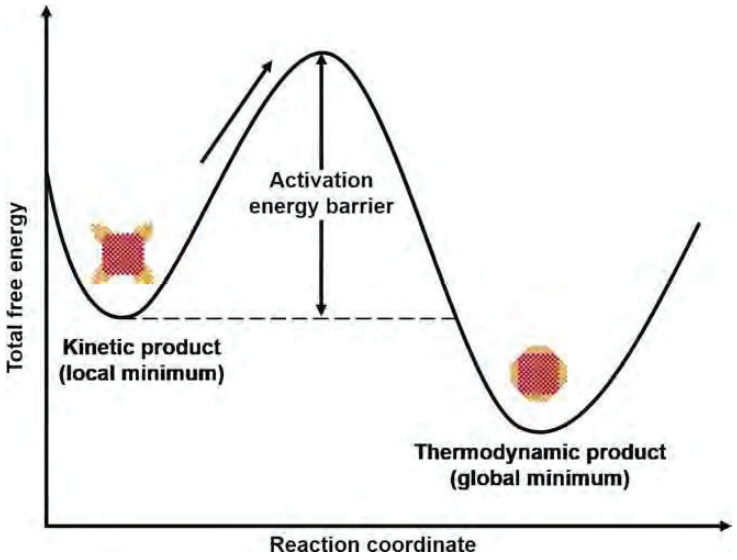

Figure 2.2: Schematic illustration of kinetic and thermodynamic NP products with relation to the total free energy. The arrow marks the activation energy required to transform a kinetic product to a thermodynamic product. Copyright (2020) Wiley. Used with permission from Ref. [30].

Capping agents can influence both the thermodynamic and kinetics by selective adsorption to crystal facets, and thus anisotropically change the surface free energies. By lowering the activation energy for a specific facet through selective adsorption, the capping agent can direct the growth into a specific shape [23,25]. Figure 2.3b visualizes an example of the role of the capping agent in the growth of a metal NP into different shapes. When a capping agent selectively passivate the (100) facets, the NP grow into a cube, whereas a different capping agent that passivates (111) facets directs the growth into an octahedral shape. Furthermore, by selective adsorption the capping agent can physically block a certain crystal facet and direct the NP shape through kinetic control.

In NP synthesis, kinetics and thermodynamics are not separate events and are often closely connected. Among the different reaction parameters, temperature has the most power in determining if thermodynamic or kinetic control is dominating in NP synthesis. Hence, a significant rise or decrease in temperature can switch the reaction from thermodynamic to kinetic control [25, 27].

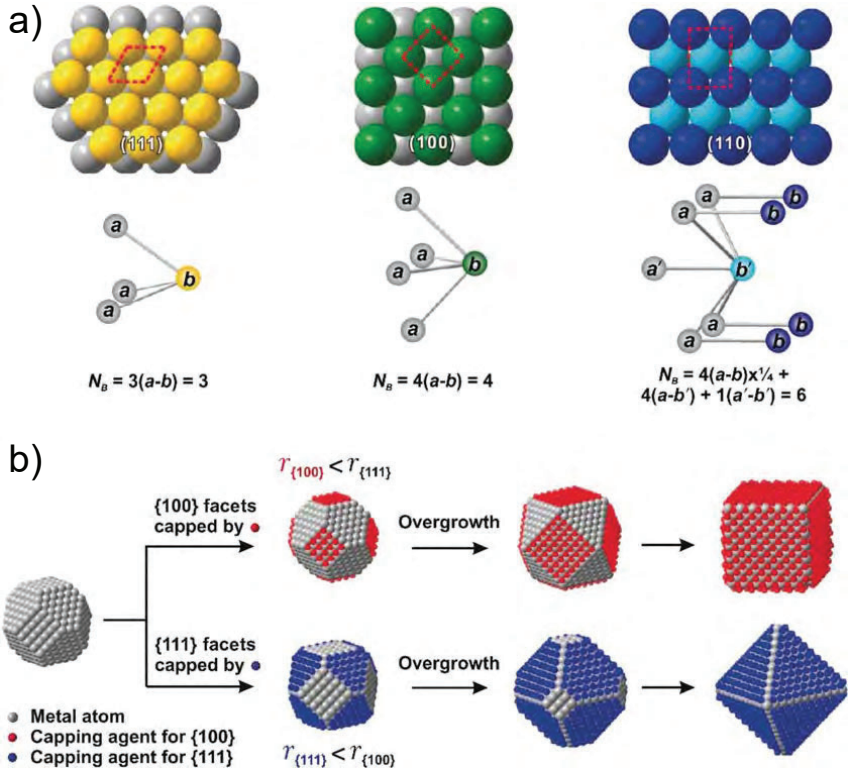

Figure 2.3: a) Models of the (111), (100), and (110) planes of a fcc-metal and the corresponding numbers of dangling bonds per surface unit cell (N_B). b) Schematic illustration of the role of a capping agent in directing the growth of a single-crystal seed into NPs with different shapes. Reprinted with permission from Ref. [27]. Copyright (2015) American Chemical Society.

2.1.2 Bimetallic nanoparticles

Due to their interesting properties, bimetallic metal NPs have been intensively studied in recent years which has led to the development of a plethora of different structures [32–41].To simplify, bimetallic NPs can be divided into two main structures, core-shell or alloy NPs. In the synthesis of bimetallic NPs, elemental composition and shape-control is more complex than for single metal NPs. Generally, the reduction can be performed simultaneously, or by a two-step seed-growth [32, 33]. The co-reduction approach can create either alloys or core-shell NPs, whereas the two-step seeded-growth normally provides core-shell structures unless significant kinetic energy is provided. I limit this section to introducing the co-reduction approach, since it is more relevant for the experimental part of this thesis.

In colloidal synthesis of bimetallic NPs, apart from the parameters mentioned previously, several factors are important in determining NP shape and composition including redox potentials, interfacial energy, and metal precursor reduction rates [32, 33, 35]. The standard reduction potential is a quantitative measure on how easy a metal precur-

sor can be reduced. The reduction potentials of metals can be lowered by selecting a capping agent that strongly coordinates to the metal, which slows down the reduction rate. The interfacial energy is determined by two factors, lattice mismatch between the two metals and the bond between the substrate metal and the surface atoms. A large lattice mismatch will lead to large lattice strain and high interfacial energy. Hence, a small lattice mismatch such as for Pd and Pt (0.77 %) facilitates the combination process [32]. Finally, the reduction rate is determined by several factors such as reduction potential, reductant and reaction temperature. By manipulating the reduction kinetics, the shape and the elemental composition of a NP can be altered from a core-shell structure to an alloy [32, 35, 37]. In a one-pot synthesis at slow reduction rate conditions, the metal with the highest reduction potential will be reduced prior to the other metal, thus creating a core-shell structure. In contrast, high reduction rates normally favors the formation of alloy NPs [32, 35].

2.2 Flow synthesis of nanoparticles

The production of colloidal metal NPs using traditional batch reactors is often limited to small scale due to challenges with reproducibility in large reactors. A possible solution is the use of flow reactors, where reagents are pumped through micro- or millimeter sized channels for a certain reaction time and temperature. The high surface area-to-reaction volume provides fast heat transfer and the small reaction volumes gives excellent mass transfer and rapid mixing, and metal NPs can be formed in a short amount of time[15–17, 42–44].

One type of flow reactor is the single-phase reactor which was designed in Paper III. In this single-phase reactor (Figure 2.4a) the flow is in the laminar regime and reactants are mixed mainly by diffusion. This creates a parabolic velocity profile that gives rise to residence time distributions inside the reactor and may result in wide particle size distributions[45–47]. A frequent challenge in single-phase flow reactors is fouling, i.e. the deposition of NPs on the reactor walls. Fouling is caused by heterogeneous nucleation and uncontrolled NP growth at the reactor walls, which could be explained by a high affinity between the reagents and the reactor. Reactor fouling causes wide particle size distributions and product losses, and will eventually result in channel clogging and reactor failure[45–47].

An approach to remedy fouling is to synthesize NPs in biphasic reactors, so called segmented flow reactors[8, 14, 18, 46, 47]. In the segmented flow reactor (Figure 2.4b), the reaction phase is infused into an immiscible carrier phase which creates sub-microliter sized droplets or segments of reaction phase. Fouling can be significantly reduced in the segmented flow reactor since contact between the reaction phase and the reactor wall

is minimized. Additionally, the efficient turbulent mixing inside the segments created by the slip velocity between the reaction phase and the carrier phase minimize axial dispersion effects normally encountered in single-phase reactors that cause wide particle size distributions[46, 47]. While fouling is reduced in segmented flow reactors, the carrier phase generates large amount of solvent waste. A recycling strategy can be implemented by separating the immiscible phases by polarity using liquid-liquid phase separation[46,48]. This approach is applied in Paper IV, where the organic carrier phase can be separated and reused in the synthesis.

Contrary to batch reactors that are limited to small production scales due to poor reproducibility, flow reactors can successfully be scaled up[15, 49]. Scale-up can be achieved by operation of the reactor for extended operation times, by reactor parallelization [15, 18, 19], or increased flow channel dimensions [13, 20, 44]. The possibility of full automation of the process enables an effective, safe and sustainable production[14, 15, 18]. NP production scale-up is studied in a single-phase reactor (Paper III) and in an automated segmented flow system (Paper IV). Furthermore, the integration of inline quality control can provide process control by the monitoring of NP growth to provide valuable data of reaction kinetics and synthesis outcome[16, 21, 44, 46, 49]. There exist several examples of inline quality measurements applied during metal NP flow synthesis including dynamic light scattering [50], UV-Vis spectroscopy [13, 50–53] and small angle x-ray scattering (SAXS) [51], that can provide structural and/or elemental information [21, 46]. However, inline quality control is currently limited for fully automated segmented flow production of Au NPs and is studied in Paper IV.

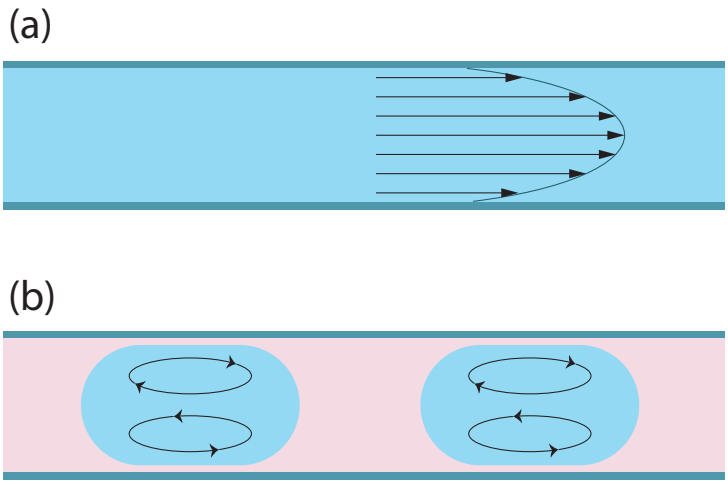

Figure 2.4: Mixing characteristics in a) single-phase laminar flow, b) segmented flow with turbulent mixing in segments.

2.3 Pd and Pt nanoparticles in catalysis

Noble metals including Pd and Pt NPs are important industrial catalysts in a range of reactions[11]. These rare noble metals are limited resources with extremely low abundance in the earths crust, notably at parts per billion concentrations [54]. The increasing demand of these scarce metals has sparked the development of more high-performing catalysts to optimize the use of these metals. The catalytic performance, i.e. reactivity and selectivity is closely related to NP size and shape, crystal facets and elemental composition. By applying shaped NPs with enhanced catalytic properties, the catalytic loading can be reduced which leads to lower costs and provide a more sustainable use of these rare metals[8]. However, in order to enhance NP catalyst performance for a certain reaction, understanding of the correlation between NP properties and catalytic activity and selectivity needs to be improved.

Shaped Pd and Pt-based NPs have been studied as catalysts in several reactions including reduction and oxidation reactions in fuel cells, carbon-carbon bond formation and hydrogenation reactions[11]. Especially interesting is the combination of Pd and Pt into bimetallic NPs, which may not only combine the individual properties but could enhance the catalytic performance and temperature stability due to synergy effects between the metals[33–35, 55]. In Paper III catalytic evaluation of Pd NCs and PdPt NPs with a core-shell structure is performed, where the effect of shape and elemental composition on catalytic activity and selectivity in a model NO_2 reduction reaction is evaluated.

Chapter 3

Synthesis and characterization methods

3.1 Colloidal synthesis and kinetic evaluation

To evaluate the effect of different reagents including stabilizers and reductants, and their influence on NP synthesis outcomes, different solution-based colloidal synthesis methods were developed and evaluated. This section describes the synthesis methods that were developed to produce Cu NPs (Paper I) and Pd NPs (Paper II), and the evaluation of reduction kinetics of Pd NPs (Paper II).

3.1.1 Synthesis of Cu and Cu_2S nanoparticles

The synthesis of Cu NPs was performed under N_2 atmosphere using a Schlenk line (Paper I). A scheme for the reaction can be found in Figure 3.1. First, the copper precursor ($CuCl_2$*$2H_2O$) was dried into brown copper chloride ($CuCl_2$) powder by heating to 60 °C for 30 minutes. Subsequently, the stabilizer dodecane thiol and solvent, dodecane, were added to the flask, and the mixture was heated to 145 °C forming a yellow dispersion. The reducing agent, tert-butylamineborane complex (TBAB) was added and the reaction was left to proceed for 5-90 min. The black Cu NP dispersion was then left to cool in room temperature. For the synthesis of Cu_2S NPs the Cu NP dispersion was reheated to 175 °C for 2 hours or left overnight under N_2, giving an orange Cu_2S NP dispersion. NP dispersions were transferred to N_2-filled centrifuge tubes filled with degassed ethanol, were centrifuged and the supernatant was discarded. The procedure was repeated twice, followed by drying in N_2 followed by dispersion in dry toluene. A detailed description of the synthesis steps and the purification of the NPs is explained in Paper I.

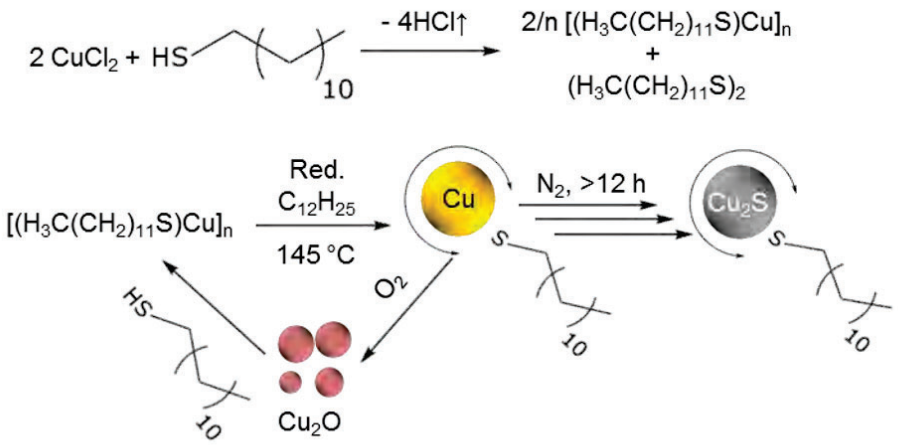

Figure 3.1: (Top) Reaction Scheme of the reaction of $CuCl_2$ and dodecane thiol yielding Cu(0)-dodecane thiol and didodecyl disulfide. (Bottom) Formation of metastable thiolate-capped Cu NPs and their decomposition paths forming Cu_2S and Cu_2O, in the presence of excess thiol under ambient conditions or N_2 atmosphere, respectively. Reprinted with permission from Ref. [56]. Copyright (2017) American Chemical Society.

3.1.2 Synthesis and reduction kinetics of Pd nanoparticles

Synthesis of Pd NPs stabilized with sodium oleate (NaOL) and hexadecyltrimethylammonium chloride (CTAC) was performed in batch (Paper II), and in the absence of traditional reducing agent. Briefly, in a vial solutions of CTAC, NaOL and H_2PdCl_4 were mixed, which created a turbid orange suspension. The vial was capped and placed in a heated convection oven for 4h, which gave a black Pd NP suspension.

UV-Vis spectroscopy was used to evaluate the reduction kinetics of Pd NPs. Samples of the reaction solution were taken at specific time points during the reaction (5-300 min), and were added to room temperature saturated KCl-solution and mixed. Aliquots of this stock solution was added to 3 Eppendorf tubes containing KCl-solution. Dilution with KCl solution was performed to avoid hydrolysis of the $PdCl_4^{2-}$ complex and to quench the reaction. The final solutions were centrifuged to separate Pd NPs from the $PdCl_4^{2-}$ complex, and the supernatant was analyzed with UV-Vis spectroscopy. The percentage of $PdCl_4^{2-}$ remaining in the reaction solutions was calculated from a standard plot. A detailed description of the synthesis and kinetic evaluation can be found in in Paper II.

3.2 Flow synthesis of nanoparticles

This section describes the flow syntheses which were developed to synthesize Pd NCs and PdPt core-shell NPs using a single-phase flow reactor (Paper III), and Au NPs using a segmented flow reactor (Paper IV).

3.2.1 Single-phase flow synthesis of Pd nanocubes and PdPt nanoparticles

Synthesis of Pd NCs was first established by adapting a batch protocol from Niu et al[57], to a micro-sized single-phase flow synthesis (Figure 3.2). Two streams of solutions were infused in micro-sized polytetrafluoroethylene (PTFE) tubing (inner diameter 800 μm) at a constant flow rate by the use of syringe pumps, interfaced in a t-junction followed by heating in a temperature controlled water bath for a certain residence time. The NP dispersion was then collected and purified by centrifugation. In the synthesis of Pd NCs, the first stream contained an aqueous solution of Pd-precursor (H_2PdCl_4) and stabilizer, hexadecyltrimethylammonium bromide (CTAB), which was reduced by a second stream consisting of an aqueous solution of reducing agent (L-Ascorbic acid). To synthesise PdPt NPs the first stream was composed of an aqueous solution of CTAB and a combination of Pd-precursor(H_2PdCl_4) and Pt-precursor(H_2Cl_6Pt) with varying molar ratios of the metals. A detailed description of the flow synthesis method and the purification steps can be found in Paper II.

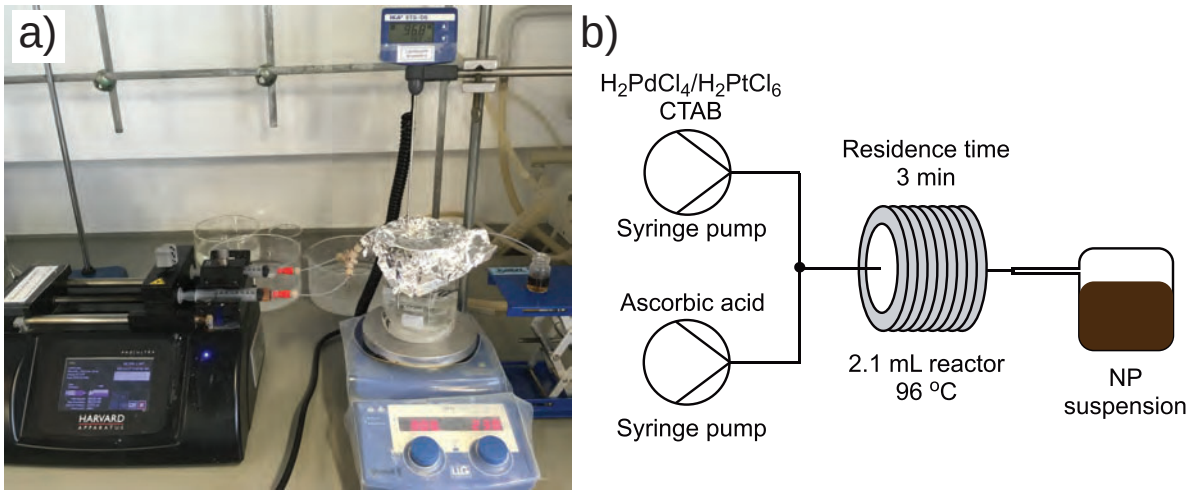

Figure 3.2: The single-phase flow system used to synthesize Pd NCs and PdPt NPs. a) Photograph of the equipment, b)Schematic setup.

3.2.2 Continuous segmented flow synthesis of Au nanoparticles

A continuous segmented hydrothermal flow synthesis was developed to produce citrate-capped Au NPs, adapted from a modified Turkevich method in batch by Kettemann et. al [58]. The segmented flow system (Figure 3.3) featured two peristaltic pumps, an ultra-smooth flow chemistry syringe pump, automated back-pressure control and full automation control using the connected computer with integrated software. The reagents were pumped in high purity grade perfluoroalkoxy (PFA) tubes. Aqueous citrate solution was interfaced with Au-precursor solution in water in an Ethylene tetrafluoroethylene (EFTE) T-junction. The outlet was connected to a glass-capillary connected to a second t-junction (EFTE). Microliter sized segments were produced when carrier phase, Isopar^{TM} L was infused to the second T-junction. The outlet of the T-junction was connected to a coiled tube microreactor (PFA), heated by hot air to a constant temperature. The outlet of the flow reactor was connected to an automated active back-pressure regulator to maintain constant pressure in the reactor and avoid gas formation. The aqueous reaction phase was separated by a liquid-liquid separator, and the organic carrier phase Isopar^{TM} L was reused in the synthesis. An inline UV-Vis spectrometer flow cell was used to monitor the quality of Au NPs in the reaction phase. The carrier phase Isopar^{TM} L was kindly sponsored by ExxonMobil. A detailed description of the segmented flow setup and experimental parameters can be found in Paper IV.

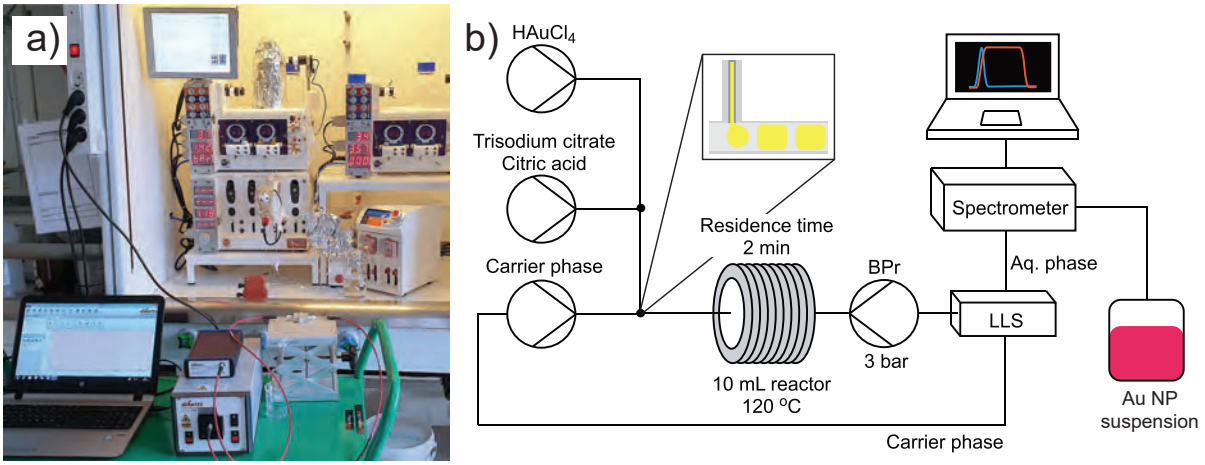

Figure 3.3: Setup of the automated segmented flow reactor for the synthesise of citrate-capped Au NPs with liquid-liquid phase separation and inline optical spectroscopy quality control, a) Photograph of the equipment, b) Schematic setup.

3.3 Characterization of nanoparticles

The synthesized NPs were analyzed with respect to morphology, size, crystal structure, elemental composition and catalytic activity using the characterization methods described in this section.

3.3.1 Transmission electron microscopy

Characterization of the morphology, size, crystal structure and elemental distribution of the synthesized NPs in Paper I-IV were studied using transmission electron microscopy (TEM). The electrons in the TEM are accelerated by a high voltage, 200-300 kV, which results in a very small wavelength. Compared to an optical microscope where the spatial resolution is limited to the wavelength of the visible light, the TEM provides significantly higher spatial resolution that can be as low as 0.1 nm dependent on various effects including instabilities and lens abberations[59]. In the TEM, an electron beam is transmitted through a very thin sample by the focusing of a series of magnetic lenses. An area of the sample is illuminated by the electron beam, and the objective lens provides an image of the area which is magnified by the projector lenses and a highly magnified image of the sample can be observed on a viewing screen or by a camera. With the use of an aperture, the selected area electron diffraction (SAED) pattern of the NPs can be recorded in the back focal plane of the objective lens[59]. By comparison to known crystal structures determination of crystal facets of the NPs can be detected. SAED was used to determine the crystal structure of Cu NPs (Paper I), Pd NPs (Paper II) and Au NPs (Paper IV).

In Scanning TEM (STEM) the electron beam is focused to a small spot and scanned over the specimen, and the intensity of the scattered electrons is recorded by a high angle annual dark field (HAADF) detector, which is atomic number sensitive and thus provides qualitative information of the sample[59]. In Paper III STEM-HAADF was used in the imaging of Pd NCs and PdPt core-shell NPs.

Interactions between the electron beam in the TEM and the sample produces a range of secondary signals providing elemental information from the NP sample. Energy dispersive x-ray spectroscopy (EDX) records the emission of characteristic x-rays resulting from the inelastic scattering of electrons in the atoms of the sample. A spectrum can be constructed with characteristic peaks that corresponds to individual elements in a selected area of the sample, which can be converted to quantitative data of the elemental distribution in the sample[59]. In Paper I, EDX was used to study the elemental composition in Cu NPs and in Paper III to determine the relative elemental distribution in PdPt core-shell NPs.

3.3.2 Scanning electron microscopy

In the Scanning Electron Microscope (SEM), an electron beam focused by magnetic lenses is scanned over the sample surface in a raster pattern. When the electron beam interacts with the electrons in the sample excited secondary electrons are created which can be detected and a topological image of the sample constructed[60]. SEM imaging of NP samples can provide information about particle shape and morphology. In Paper III, SEM imaging was performed on Pd NCs and PdPt core-shell NPs deposited onto Si-substrates to study the effect of heat treatment on NP morphology.

3.3.3 Ultraviolet-visible spectroscopy

Ultraviolet-visible (UV-Vis) spectroscopy is a technique used to measure absorbance of molecules that undergo electronic transitions in the ultraviolet and visible light range. Quantitative measurements can be used by following the Lambert-Beer law stating that the absorbance is related to the concentration of the analyte and the path length of the light. The wavelength of the absorbance peak can be used to analyze metal NPs, and metal precursor complexes present in solution[61]. When metal NPs interact with incoming light, excitation of the surface plasmons gives rise to absorption and excitation events. This in turn creates different perceived colors of the NP suspension, determined by the chemical environment and composition. The position and width of the absorption peak in the spectrum can provide information of shape, size and elemental composition of the NPs[62]. In Paper II, a quantitative evaluation of the reduction kinetics in the synthesis of Pd NPs was studied with UV-Vis spectroscopy. Cu NPs were analyzed with UV-Vis spectroscopy under N_2 atmosphere to study the stability over time (Paper I), and inline quality control using UV-Vis spectroscopy was applied to continuously monitor the consistency of flow-synthesized Au NPs (Paper IV).

3.3.4 Powder x-ray diffraction

In powder x-ray diffraction (XRD), a powder sample is irradiated with an X-ray beam scanned at different incident angles which interacts with the electrons in the sample and result in different scattering intensities at various angles. The resulting diffraction pattern can be identified by comparison to a known standard or a database[63]. XRD was applied to study the changes in the crystal structure of Cu NPs that over time formed Cu_2S NPs (Paper I).

3.3.5 Microwave plasma atomic emission spectroscopy

Microwave plasma atomic emission spectroscopy (MP-AES) is an atomic emission technique that was used to quantify the synthesis yield for batch and flow synthesized Pd NCs (Paper III). Microwave plasma excites the elements in the sample and an emission spectrum with characteristic wavelengths for a specific element can be created. The intensity of the emitted light is proportional to the number of atoms, and qualitative and quantitative information about the elements in the sample is provided [64]. To quantify the Pd content in Pd NC suspensions (Paper III), the emission spectrum of completely dissolved Pd NP solutions were compared to standards with known Pd concentration.

3.3.6 Fourier transform infrared spectroscopy

In fourier transform infrared (FTIR) spectroscopy an infrared source is interacting with a sample which cause molecular vibrations and absorbance. The infrared source is scanned over a wide spectral range to produce an absorption spectra. In a molecule, the atoms absorb frequencies that are characteristic of their structure, depending on their mass and arrangement. Since every molecule has slightly different vibration mode, the spectrum produced is unique and can be used to identify and study chemical compounds[65]. In Paper II, FTIR spectroscopy with an attenuated total reflection (ATR) diamond crystal was used to study the chemical composition of reagents and Pd NPs.

3.3.7 Nuclear magnetic resonance

Nuclear magnetic resonance (NMR) is a technique to study local interaction between magnetic moment of atomic nuclei and an external magnetic field. A radiofrequency transmitter excites the nuclei, creating magnetic resonance of the nuclei, and the signals are detected by a receiver and recorded as spectral lines. A spectrum can be generated for compounds containing atoms with non zero magnetic movement, such as the proton ^{1}H. In a molecule, the magnetic resonance of an atom is dependent on the magnetic field of the surrounding atoms. Thus, NMR can provide detailed information about the electronic structure and individual functional groups in a molecule. Since the magnetic field is characteristic for a certain compound, NMR can be used for identification and can provide structure determination of unknown samples, study dynamics, reaction mechanisms, and chemical environment[66]. In Paper II, ^{1}H NMR was used to study the structure and chemical environment of the reagents NaOL, CTAC and Pd NPs.

3.3.8 Zeta potential

Zeta potential can be applied to evaluate the surface charges of NPs. When a charged particle is dispersed in a solvent, an adsorbed electrical double layer forms at its surface. The layer closest to the particle is of opposite charge to the particle, referred to as the Stern layer. Due to the electrostatic field of the NPs a diffuse layer consisting of opposite and same charge as the particle form on top of the Stern layer. Together with the Stern layer this forms the electrical double layer. Application of an electric field results in charges in the diffuse layer moving towards the opposite electrode. The slipping plane is a hypothetical plane acting as an interface between the moving charges and the dispersant around them, and the zeta potential is the potential at this interface[67]. Zeta potential was used to evaluate the colloidal stability of Au NPs (Paper IV).

3.3.9 Catalytic evaluation

In Paper II, Pd NCs and PdPt core-shell NPs were evaluated as catalysts in the NO_2 reduction reaction. The flat samples were assembled in a tube "pocket reactor", previously described by Bu et al[68]. Catalyst samples were prepared by drop casting concentrated NP suspension onto plasma-treated fused silica substrates. The NP samples were first pre-treated under a gas flow and heated (150 °C), and cooled down to 48°C. The samples were then exposed to the reaction mixture (2200 ppm NO_2 and 2.2 % H_2 in argon) with the temperature gradually ramped up to 136 °C. The outlet gas composition was detected by mass spectroscopy, and the conversion and product selectivity quantified. A detailed description of the experimental setup can be found in Paper III.

Chapter 4

Results and discussion

4.1 Stabilizer effects and reduction mechanisms for colloidal nanoparticles

This section focuses on the multiple roles of the stabilizers in NP synthesis and how they can influence NP properties. I investigated the role of the stabilizers in the synthesis of Cu NPs and the subsequent formation of Cu_2S NPs (Paper I), and in the synthesis of Pd NPs stabilized with a binary surfactant combination (Paper II). Furthermore, quantitative evaluation of reduction kinetics in the synthesis of Pd NPs (Paper II) was evaluated to investigate the mechanisms involved in the synthesis.

4.1.1 Multiple roles of stabilizers

In Paper I, I developed a synthesis of spherical Cu NPs (3-10 nm) and investigated their stability and elemental composition over time. A range of reaction parameters and the effect on the particle size distributions were evaluated. The uniform Cu NPs (Figure 4.1a) consist mainly of Cu(0) and CuO species that formed after oxidization of the NPs on the TEM-grid, which is confirmed by SAED (Figure 4.1b). When exposed to ambient atmosphere, the Cu NPs oxidized and the color of the NP suspension changed from black to brown along with the disappearance of the plasmon resonance maximum at 597 nm. The Cu NP suspensions were not stable for more than 12h even under protected N_2 atmosphere and showed aggregation and precipitation. Interestingly, under N_2 atmosphere the Cu NP suspension changed color from blue to orange, despite the absence of oxygen, and showed poor colloidal stability. To evaluate the effect of temperature, the Cu NP suspension aged at room temperature was heated to 175 °C which yielded uniform Cu_2S NPs (Figure 4.1c). SAED of the NPs shows the presence of hexagonal Cu_2S and Cu (0) species, but no Cu(I)O (Figure 4.1d).

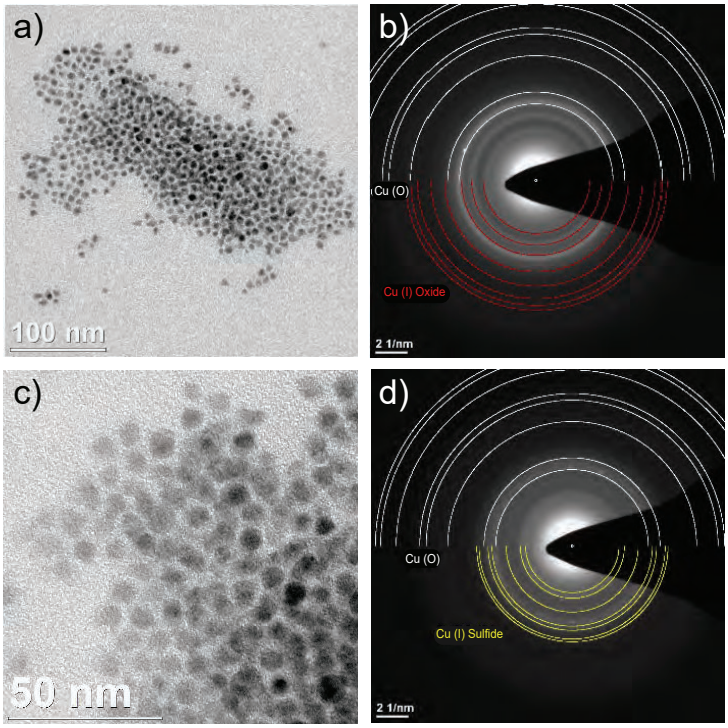

Figure 4.1: TEM images of a) Cu NPs, c) Cu_2S NPs. b) and d) shows the corresponding SAED of the NPs from a) and b), respectively. Reference patterns of Cu(0), JCPDS-Nr. 4-0836 (white semicircles), Cu_2O, JCPDS-Nr. 5-0667 (red semicircles), and hexagonal Cu_2S, space group P63/mmc, JCPDS-Nr. 46-1195, (yellow semicircles). Adapted with permission from Ref.[56]. Copyright (2017) American Chemical Society.

The stability of freshly synthesized thiolate-protected Cu NPs in N_2 atmosphere was evaluated by UV-Vis spectroscopy (Figure 4.2). With time (0-275 min), a gradual disappearance of the plasmon resonance band occurred and the peak maximum slowly decreased and shifted to longer wavelengths, however at a much slower rate than previously reported for oxidation of Cu[69]. It can therefore be excluded that the diminishing absorbance maximum was caused by Cu NP oxidation, but may instead be a result of NP aggregation. The presence of sulfur in the Cu NP samples was confirmed by EDX analysis. However, EDX and XRD analysis on the samples aged at room temperature could not detect crystalline Cu_2S species. XRD analysis of the heated Cu NP suspension on the other hand shows the presence of hexagonal Cu_2S phases. Therefore, it can be concluded that Cu_2S were not formed in room temperature, and heating of the NP suspension was necessary to yield crystalline Cu_2S NPs, or Cu NPs coated with a Cu_2S shell.

These findings point to the general conclusion that the thiolate stabilizers can not provide sufficient colloidal stabilization of Cu NPs under longer time in room temperature, even under protected atmosphere. Furthermore, heating of the suspension was necessary to form crystalline Cu_2S NPs. As the only sulfur source in the Cu NP synthesis,

it can be concluded that during heating of the Cu NP suspension, the alkane thiolate stabilizer decomposed through cleavage of the C-S bond at the surface of the Cu NPs, and only provided temporary stabilization of the Cu NP surface. This agrees well with previous findings by Vollmer et. al [70].

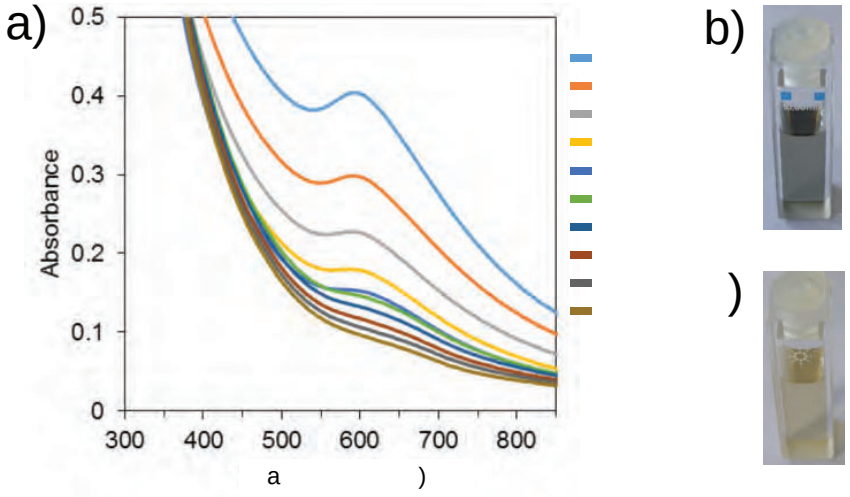

Figure 4.2: (a) Temporal evolution of UV-Vis absorption spectra of freshly synthesized Cu NP suspension. Photograph of the Cu NP suspension after b) 0 min, and c) after 275 min. Adapted with permission from Ref. [56]. Copyright (2017) American Chemical Society.

Apart from decomposing on the surface to alter the chemical composition of NPs, the stabilizer can have other roles in the synthesis of metal NPs. In Paper II I investigated the influence of the stabilizers in the development of a synthesis of Pd NPs stabilized with a binary surfactant mixture of NaOL and CTAC. The synthesis was performed in the absence of traditional reducing agents, hence the Pd-precursors were reduced spontaneously in the reaction mixture at 100 °C. Based on earlier findings [71], our initial hypothesis was that the electron dense alkyl double bond in the stabilizer NaOL was the main contributor to the reduction of Pd-precursors. After 4 hours of reaction uniform Pd NPs formed (Figure 4.3) with an average size of 29.7 nm $\pm$ 5.7 % (Inset in Figure 4.3a). The Pd NPs are polycrystalline, seen by multiple diffraction rings (inset (Figure 4.3b), and can be visualized in the HRTEM image of a single multiple-twinned Pd NP (Figure 4.3c,d).

A range of reaction parameters were investigated to study the influence on the Pd NP properties, thoroughly described in Paper II. In this thesis I focus the discussion on the effects of altering the stabilizers on Pd NP properties. To evaluate the hypothesis that the double bond is responsible for the reduction of Pd-precursors, NaOL was replaced with the structurally similar saturated fatty acid, sodium stearate (NaST). Surprisingly, this stabilizer combination could also produce Pd NPs, which are smaller than

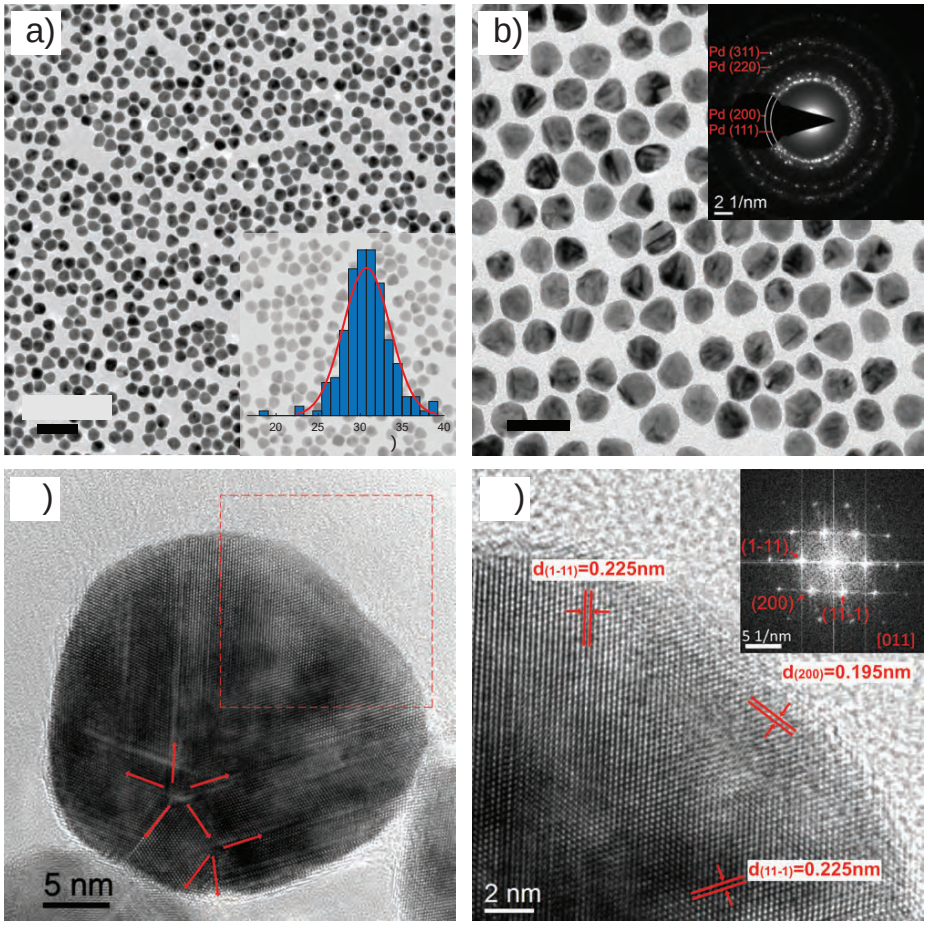

Figure 4.3: Structural characterization of Pd NPs stabilized with NaOL and CTAC. a),b) TEM images of monodisperse Pd NPs at relatively low magnification, where inset in a) shows histogram of particle size distribution with an average size of 29.7 nm $\pm$ 5.7 %, inset in b) shows the SAED pattern of Pd NPs. c) HRTEM image of an individual Pd NP shows a multiple-twinned structure, where twin boundaries are marked with red arrows, d) HRTEM image of the selected area of the Pd NP marked by a red square in c). The inserted image in d) shows a corresponding FFT pattern.

with NaOL, with an average size of 13 nm $\pm$ 19 % (Figure 4.4a). The reaction was slower than with NaOL, observable by a later color change of the reaction solution. The reduction speed was further investigated with UV-Vis spectroscopy, as explored in the following section. Reduction occurred despite the NaST lacking double bonds which indicates that the reduction mechanisms are more complex than the previously proposed hypothesis.

When CTAC was replaced with CTAB, the equivalent ammonium salt with bromide as counter ion in the surfactant mixture, Pd NPs with different shapes formed (Figure 4.4b). This includes bars, cubes and "arrow" shaped Pd NPs. After 4 hours reaction, excess particle seeds are present and Pd NPs are smaller than than those stabilized with

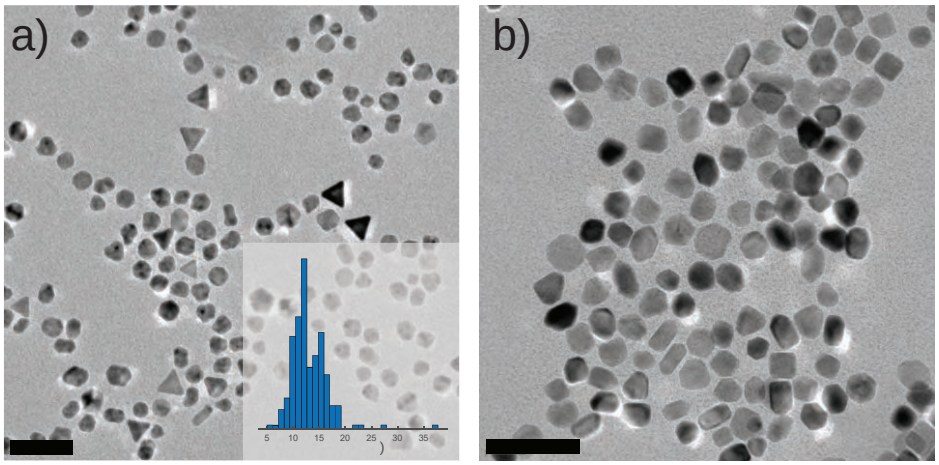

Figure 4.4: a) TEM image of Pd NPs stabilized with NaST and CTAC, where Inset in a) shows a correspoding histogram of size distributions with an average size of 13 nm ± 19 %. b) TEM image of Pd NPs stabilized with NaOL and CTAB.

NaOL and CTAC (Figure 4.4b). Despite using the same reductant (NaOL), a slower reduction was evidenced by a slower color change of the reaction solution. The difference in shapes obtained when CTAC was replaced with CTAB could be due to bromide ions (Br^-) present in CTAB, well-known to selectively adsorb onto (100) crystal facets and have been applied extensively in the controlled synthesis of cubic [57, 72] and rod-shaped Pd NPs [73]. In the synthesis of CTAB-stabilized Au nanorods, Meena et. al [74] showed that Br^- adsorption is not the only contributor to the selective surface passivation of (100) facets, but is a driving force for CTAB micelle adsorption and stabilization of the Au nanorod surface. CTAB was shown to form dense surfactant micellar layers on gold surfaces. In contrast, more isotropic shaped particles were obtained with CTAC, due to less facet selectivity and the low presence of Cl^- and micellar structures protecting the Au surface. These findings may explain the difference in shapes observed when CTAC was replaced with CTAB in the synthesis of Pd NPs. Furthermore, the slower reduction of Pd-precursors observed in the presence of CTAB could partly be explained by the strong complexation between bromide ions in CTAB and Pd-precursors ($PdBr_4^{2-}$). Additionally, the dense and thick surfactant layer of CTAB may lower the accessibility of NaOL to reduce Pd-precursors which could contribute to a slower reduction rate.

In order to produce colloidally stable Pd NPs it was necessary to use a binary stabilizer combination with the anionic surfactant NaOL/NaST and the cationic surfactant CTAC. When synthesis was performed in the absence of CTAC, reduction occurred and Pd NPs formed but the stabilizers (NaOL/NaST) provided poor colloidal stability and extensive visual particle aggregation in solution could be observed. On the other hand, synthesis with only CTAC does not result in any reduction of Pd-precursors. These

findings lead to the conclusion that CTAC was necessary to provide sufficient colloidal stability of Pd NPs, but did not contribute to the reduction of Pd-precursors. To study the interactions between the stabilizers NaOL and CTAC with Pd NPs, qualitative analysis was performed using FTIR and NMR, which showed that the stabilizers provided colloidal stabilization by adsorption onto the NP surface. Details of the experiments and qualitative analysis can be found in Paper II. It is clear that NP stabilizers can have multiple roles in the NP synthesis and their influence of the outcomes can be complex.

4.1.2 Evaluation of reduction kinetics

To investigate the kinetics involved in the Pd NP synthesis (Paper II), a quantitative evaluation of reduction kinetics was performed by UV-Vis spectroscopy. Reduction kinetics were monitored by following the diminishing absorbance peak of $PdCl_4^{2-}$ (280 nm) over time (5-300 min). In coherence with previous observations, it is clear that the reduction of Pd precursors stabilized with NaOL and CTAC (Figure 4.5a) is faster than the combination with NaST and CTAC (Figure 4.5b). A quantitative analysis of the reduction (Figure 4.5c), reveals that after 1 hour of reaction 50.8 % of $PdCl_4^{2-}$ is reduced in the CTAC and NaOL system, which is increased to 87.2 %, and 89.4 % after 4 and 6 hours of reaction, respectively. In comparison, for the system with NaST and CTAC only 7.4 %, 15.4 % and 16.3 % $PdCl_4^{2-}$ is reduced after 1, 4, and 6 hours, respectively.

In the evaluation of reduction kinetics, several kinetic models have been developed to describe metal NP formation [28,75–77]. Since the reduction reaction in the solution-based colloidal synthesis is governed by electron transfer between a reductant and metal precursor, the reaction is normally considered bimolecular, and the rate of reaction depend on both reactants [12, 78]. As the reductant normally is supplied in excess the reaction can be simplified to a pseudo first-order reaction rate law, where the reaction rate is dependent on the concentration of the metal precursor. When the first-order reaction law is applied to the data for Pd NPs (Figure 4.5d), the two systems show adequate correlation as the plot of ln $[PdCl_4^{2-}]$ decreases linearly over time. The rate constants were calculated to $k=1.27\cdot10^{-4}$ s^{-1} for NaOL and CTAC, and $k=1.17\cdot10^{-5}$ s^{-1} for NaST and CTAC. The time points at 250 and 300 min slightly deviates from the model. It could therefore be discussed if the reduction mechanisms at this time in the reaction involve other mechanisms such as particle aggregation. For the pseudo-first order rate law, the concentration of the reductant, in our case NaOL, is assumed to remain constant throughout the reaction. For our system, the concentration of NaOL was not supplied in excess in relation to Pd-precursors. Despite this fact, our data correlate fairly well with the pseudo first-order model. It could be argued that NaOL might have the capability of reducing several Pd-ions into metallic Pd, and thereby

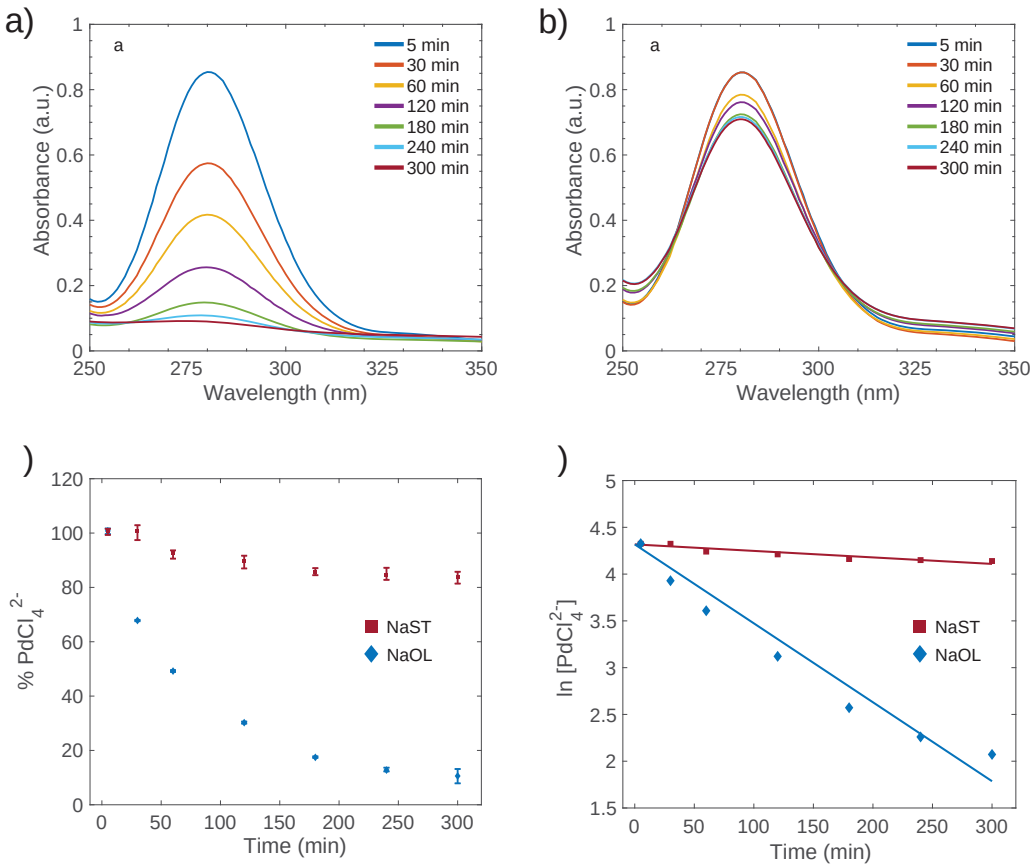

Figure 4.5: Analysis of the reduction kinetics in the synthesis of Pd NPs. UV-Vis spectra of $PdCl_4^{2-}$ in the reaction solution after 5-300 min for Pd NPs stabilized with a) CTAC and NaOL, b) CTAC and NaST. c) A plot showing the percentage of $PdCl_4^{2-}$ remaining in the reaction solutions for Pd NPs synthesized with NaOL and CTAC (blue), and with NaST and CTAC (red) measured from the absorbance peak at 280 nm as a function of time. d) Plots of ln $[PdCl_4^{2-}]$ over time, which shows the pseudo-first order reaction kinetics involved in the synthesis of Pd NPs stabilized with NaOL and CTAC, and with NaST and CTAC, respectively.

retain a constant concentration through the reaction. Since the exact mechanisms of the reduction are still not fully clear, further studies into this aspect should be performed to provide a better understanding. To evaluate the influence of the stabilizer on reduction kinetics, the effect of varying the concentration of reductant, i.e. NaOL/NaST, on the reduction kinetics could be performed. Moreover, application of the Finke-Watzky (F-W) kinetic model [75] to our data was performed since it could provide a model for relatively slow reduction reactions [12]. The F-W model describes the reduction through several steps including nucleation, homogeneous aggregation and autocatalytic surface growth. Application of the model to our data shows poor agreement, where our system presents a slow continuous reduction as opposed to the F-W model which includes a slow reduction followed by fast autocatalytic growth.

The type of metal precursor and the metal precursor and ligand coordination is known to substantially influence reduction kinetics [12, 77]. Therefore, in the synthesis of Pd NPs it would be interesting to evaluate the effect on reduction kinetics of changing type of Pd-precursor, i.e. the type of metal precursor complex. It is clear from this study that CTAC plays an important role in providing shape and colloidal stability of the Pd NPs. The effect on shape and reduction kinetics when CTAC was replaced with CTAB, caused by the stronger complexation between Pd-precursors and Br^- ions serves as a first example and it would be interesting to study other cationic surfactants and their effect on reduction kinetics and NP properties.

Another possible direction to extend investigations of reduction kinetics could be the study of other metals such as Au. Syntheses of various shaped Au NPs have been performed with traditional reducing agents and stabilization of NaOL and CTAB [71] and oleic acid and CTAB [79]. During the synthesis a noticeable color change of the Au-precursor solution have been claimed to indicate that NaOL may act as partial reducing agent for Au(III) precursors. Yet, further studies would be needed to understand the reduction kinetics and mechanisms for Au NPs in the absence of these reducing agents.

From the quantitative evaluation of the reduction kinetics involved in the synthesis of Pd NPs, it can be concluded that the alkyl double bond in NaOL is not necessary to reduce Pd-precursors. Nonetheless, it may influence the reduction rate since reduction with NaOL is faster and more effective than Pd NP synthesis with the saturated fatty acid NaST. However, the exact mechanisms governing the reduction needs to be further studied to elucidate what electron donating groups that contribute to reducing Pd-precursors. Elemental analysis of byproducts formed during NP synthesis using e.g. NMR and Mass spectroscopy may improve understanding of the mechanisms during reduction [80], which could elucidate the mechanisms involved in the reduction of Pd-precursors (Paper II) but also to understand the decomposition of alkane thiolates on the surface of Cu NPs (Paper I). The evaluation of byproduct chemistry during metal NP synthesis may be challenging since byproducts can be present in small quantities, and many reagents are involved in the synthesis (metal precursors, stabilizers, reductants etc.) which creates a multitude of possible compounds and combinations to evaluate. In this study, we applied NMR and Liquid chromatography and mass spectroscopy (LCMS) to evaluate the byproducts formed during the Pd NP synthesis. Nonetheless, these analyses led to inconclusive results and further analyses are needed to draw significant conclusions on the reduction mechanisms involved in the synthesis. Despite these results, byproduct evaluation could be a valuable tool in evaluation of NP properties and contribute in the development of metal NP synthesis procedures.

4.2 Flow synthesis of colloidal nanoparticles

The second focus of this thesis is the development of flow synthesis methods, due to their potential to provide excellent control over NP properties. First, I developed a synthesis of Pd NCs and PdPt NPs using a single-phase flow reactor (Paper III), and an automated segmented flow synthesis was developed for the production of Au NPs (Paper IV). A range of reaction parameters were evaluated and the effects of synthesis temperature discussed. Furthermore, the scale-up of NP flow production was studied, with the future aim of targeting real applications. Finally, evaluation of catalytic performance in a model catalytic reaction of Pd NCs and PdPt NPs was performed (Paper III).

4.2.1 Development of a single-phase flow synthesis

In Paper III, I developed a method to synthesize Pd NCs using a single-phase flow reactor. First, Pd NCs were synthesized in batch (Figure 4.6a) according to the protocol by Niu et al[57], and then the synthesis was translated to a single-phase flow reactor (Figure 4.6b). A range of reaction parameters were investigated to find the optimum flow synthesis conditions, including temperature, stabilizer concentration and reaction time. The STEM-HAADF image in the right inset in (Figure 4.6b) shows the [100] crystal planes of the Pd NCs. The more efficient mixing, heat and mass transfer in the flow reactor enabled a 10-time shortening of the reaction time, which resulted in smaller Pd NCs. The batch synthesized Pd NCs have a size of 27.3 nm $\pm$ 11 % (inset in Figure 4.6a),

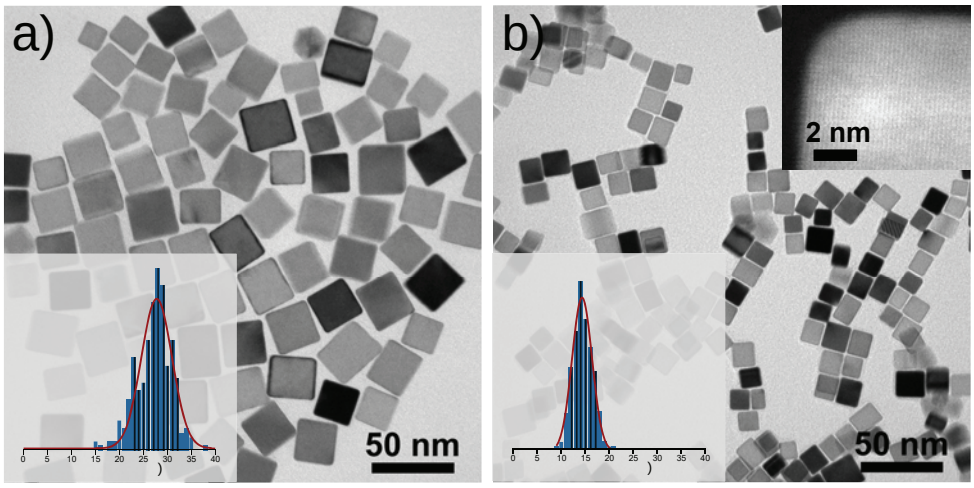

Figure 4.6: TEM images of Pd NCs synthesized in a) batch, b) in single-phase flow.The inset in b) shows a high-resolution TEM-image of a single Pd NC. The corresponding histogram of particle size distribution in inset a) shows a size of 27.3 nm $\pm$ 11 % for the batch reactor, and inset in b) 14.4 nm $\pm$ 11 % for the flow reactor.

and Pd NCs synthesized in flow 14.4 nm ± 11 % (inset in Figure 4.6b). Comparison of NP uniformity shows no significant difference between the two methods. Nonetheless, when the particle yield was examined using MP-AES, observing the amount of Pd precursor that has been reduced into metallic Pd NCs, a significant improvement in reaction yield can be seen for flow synthesized Pd NCs (94 % in flow, 63 % in batch). This improvement in synthesis yield could be explained by the more efficient heat and mass transfer in the flow reactor[43].

Motivated by the enhanced catalytic properties of bimetallic NPs, I modified the synthesis to incorporate a second metal to produce bimetallic PdPt NPs. By varying the relative molar ratios of Pd:Pt in the precursor stream, the morphology of the formed PdPt NPs can be controlled, which gradually changes from rough cubic to a spherical dendritic shape with increasing Pt concentration (Figure 4.7).

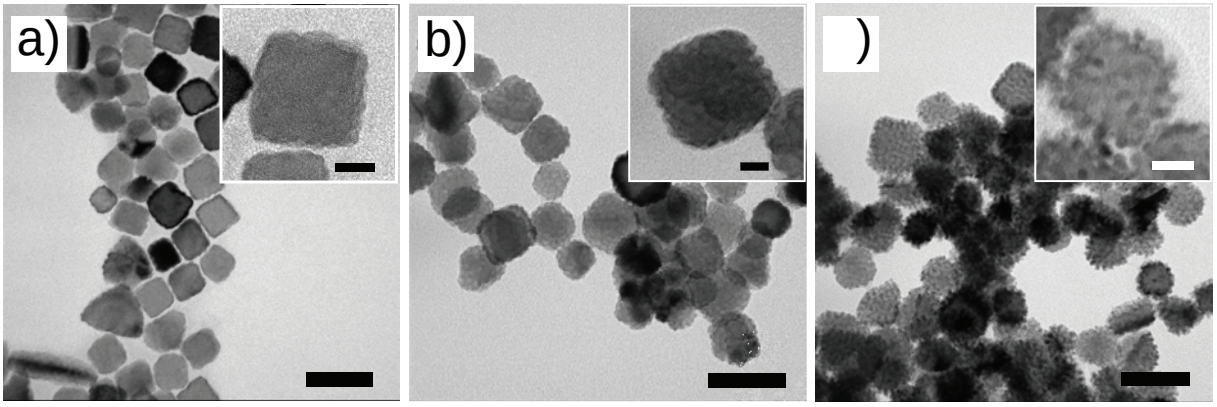

Figure 4.7: TEM-images of flow-synthesized PdPt NPs. The molar ratio of Pd:Pt in the particles are a) 6:1, b) 3:1, c) 1:1. Scale bars are 50 nm, in inset images scale bars are 10 nm. Reprinted with permission from Ref.[81]. Copyright (2019) American Chemical Society.

Characterization using STEM-HAADF of the PdPt NPs with the highest Pt concentration clearly visualizes the dendritic surface topography (Figure 4.8a,c,d). The elemental distribution, analyzed by a line scan on the NP using STEM-EDX (Figure 4.8b) reveals a core-shell structure with Pd dominated in the core and a Pt-rich surface. The formation of bimetallic NPs is directed by the kinetics and reduction potential of the two metals. Despite its lower reduction potential, Pd is reduced first to form the particle core. The slower reduction rate of Pt precursors could be explained by the stronger complexation between Pt precursors and CTAB [82], which then lead to the formation of PdPt core-shell NPs.

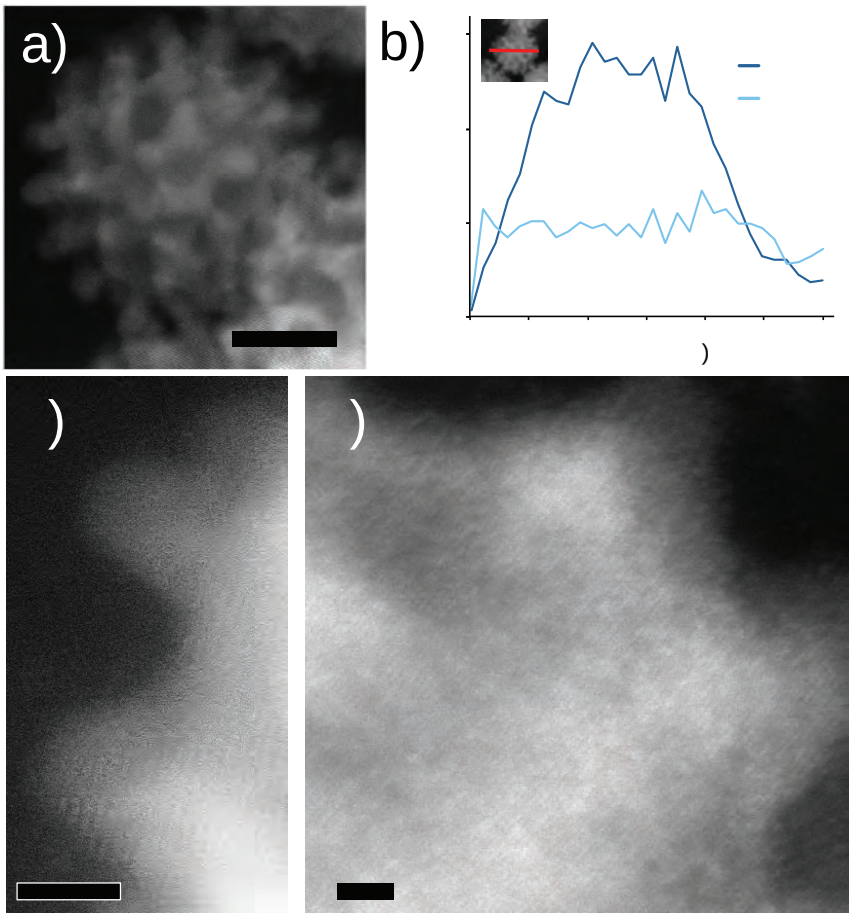

Figure 4.8: a) HAADF-STEM image of flow synthesized PdPt NPs with the highest Pt ratio. b) EDX line scan of a single PdPt NP which shows the relative distribution of Pd and Pt, a core-shell structure. c) and d) shows high-resolution HAADF-STEM images of PdPt NPs. Reprinted with permission from Ref.[81]. Copyright (2019) American Chemical Society.

4.2.2 Development of an automated segmented flow synthesis

In Paper IV, I developed a hydrothermal segmented flow synthesis of citrate-capped Au NPs. The synthesis was fully automated, and the carrier phase was separated from the reaction phase and reused in the synthesis. After 2 minutes of reaction, uniform Au NPs (Figure 4.9a,b), with a narrow size distribution of 9.5 nm $\pm$ 0.8 nm (8.4 %) (inset Figure 4.9a) were produced. The majority of Au NPs are quasi-spherical and polycrystalline seen by multiple diffraction rings (inset in Figure 4.9b) and the HRTEM image (Figure 4.9c). The size and size-distribution of Au NPs was confirmed by UV-Vis spectroscopy where the NPs show an absorbance maximum at 518 nm (Figure 4.9d). During the development of the segmented flow synthesis of Au NPs, a range of reaction parameters were evaluated including, temperature, reaction time and volume ratio of reaction phase and carrier phase.

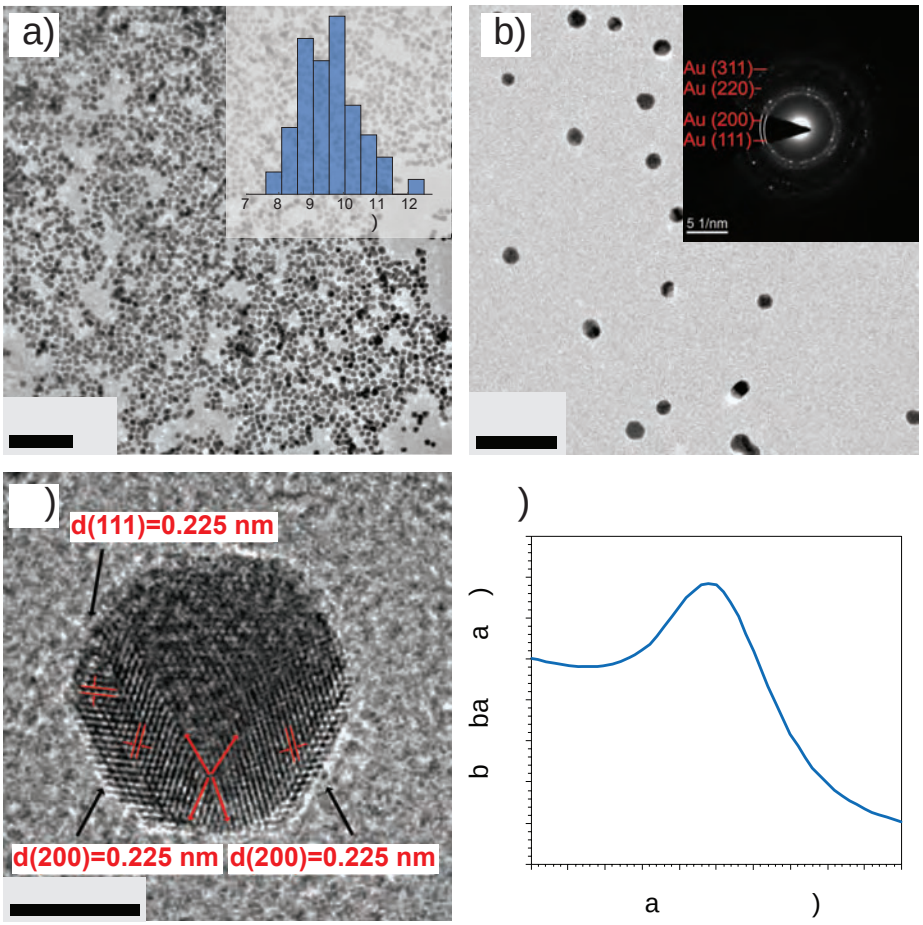

Figure 4.9: a), b) TEM images of uniform citrate-capped Au NPs at relatively low magnification. The histogram of size distribution in inset in a) shows that the Au NPs have a size of 9.5 nm $\pm$ 0.8 nm (8.4 %). The inset in b) shows the SAED pattern of Au NPs. c) HRTEM image of a single Au NP shows a polycrystalline structure, where boundaries between different crystalline domains are marked with red arrows. d) UV-Vis absorbance spectrum of Au NPs with an absorbance maximum at 518 nm.

The narrow size distribution of the Au NPs synthesized in the segmented flow reactor could be attributed to the internal back-mixing related to the slip velocity between the segments of reaction phase and carrier phase that cause turbulent mixing. This chaotic mixing eliminates axial dispersion effects normally experienced in single-phase reactor that can cause wide particle size distributions [47, 52, 83, 84]. Furthermore, our segmented flow reactor was integrated with automated back-pressure control which enables the potential to conduct the synthesis at higher pressure and temperature, so called hydrothermal conditions. A higher reaction temperature may shorten of reaction time due to a faster nucleation and growth. The segmented flow reactor enables precise controlled synthesis under hydrothermal conditions, which is not easily achieved in conventional batch reactors.

4.2.3 Flow synthesis optimization - effect of temperature

In the development of the flow synthesis of Pd NCs and PdPt NPs (Paper III), and Au NPs (Paper IV), a systematic evaluation of different reaction parameters were performed to evaluate the influence on NP properties. Details of all the tested parameters can be found in Paper III and Paper IV. Since the temperature has a big influence on reaction kinetics in the synthesis of metal NPs, directing the outcome of the synthesis [12, 27], the effect on nucleation and growth of NPs by variation of the synthesis temperature was evaluated for both flow systems.

When the temperature was lower than the optimal conditions (60 °C for Pd NCs and PdPt NPs, 100 °C for Au NPs), larger Pd NPs (Figure 4.10a), PdPt NPs (Figure 4.10c) and Au NPs (Figure 4.10e) form. When the synthesis temperature is lowered, the nucleation rate is slower which results in fewer particle seeds that subsequently grow into larger NPs. Ftouni et. al observed an increase in Au NP size when the flow synthesis temperature was reduced from 100 °C to 60 °C [85]. At the lower synthesis temperature, PdPt NPs (Figure 4.10c) formed highly dendritic and porous NPs. Pd NPs synthesized at the same temperature consisted of different shapes including nanorods, triangles, multiple twinned NPs and NCs (Figure 4.10a). The slower nucleation rate experienced at lower synthesis temperature may have increased the prevalence of Pd NP seeds with stacking faults or multiple twinned structures that subsequently direct the growth into different structures such as multiple twinned particles and nanorods. However, further structural characterization is needed to confirm the exact structures of the Pd NPs. Both thermodynamics and reaction kinetics, largely influenced by temperature, play important roles in determining the structure of NP seeds [27]. Since the shape of the NPs strongly depends on the initial structure of the seeds (presence of stacking faults, twinned structure or single-crystal), control of temperature can direct these properties [12]. Wang et. al [86] correlated the reduction rate with the structure of the seeds and found that relatively slow reduction of Pd-precursors generated seeds with stacking faults and/or twin planes, whereas higher reduction rates yielded single-crystal Pd NPs.

When the synthesis temperature was increased (130 °C for Pd NCs and PdPt NPs, 140 °C for Au NPs) various effects on sizes and shapes can be seen. Pd NCs (Figure 4.10b) have a wide distribution of sizes and shapes including rods, cubes, and twinned NPs. Plenty of the Pd NPs are smaller than the Pd NCs synthesized at the optimal conditions (96 °C). Similar size distribution effects are observed for the PdPt NPs (Figure 4.10d). The wide size and shape distributions observed for Pd NPs and PdPt NPs synthesized at 130 °C could be explained by the difference in nucleation and growth rates. The nucleation and growth are competing processes that occur simultaneously [12], and at

this temperature, the optimal parameters of nucleation and growth differ, which may cause shape and size variations. In contrast, Au NPs synthesized at 140 °C experienced extensive aggregation and formed large structures (Figure 4.10f).

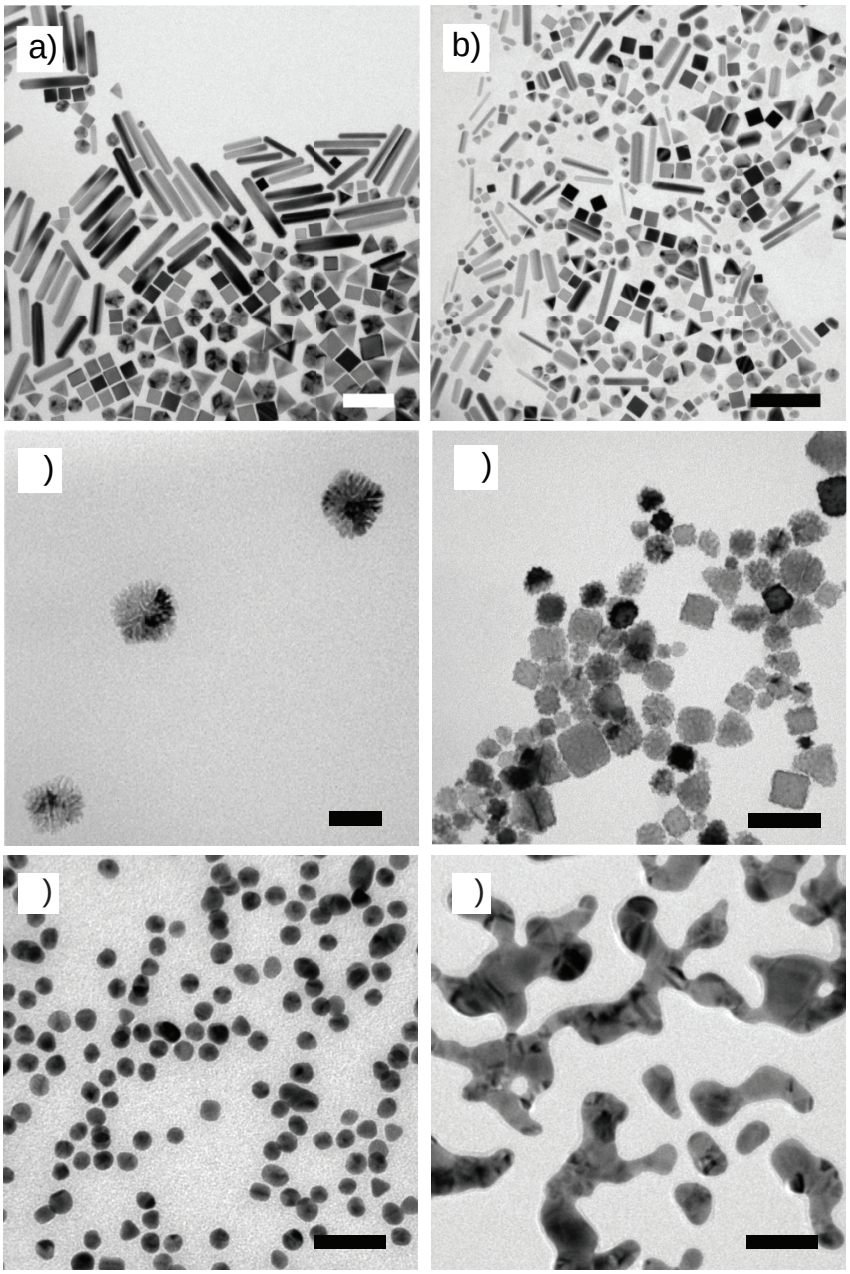

Figure 4.10: TEM images of a) Pd NCs and c) PdPt NPs synthesized in single-phase flow at 60 °C. b) Pd NCs and d) PdPt NPs synthesized in flow at 130 °C. Au NPs synthesized in segmented flow at e) 100 °C and f) 140 °C. Scale bars are 50 nm.

When the synthesis temperature was raised, the acceleration of nucleation of growth created many small NP seeds. Without proper colloidal stabilization, the citrate-capped Au NPs aggregated in an effort to minimize the high surface energy of the individual small NPs. This correlates well with previous findings [87], where nuclei aggregation

and polydisperse Au NPs can be seen when synthesis temperature was increased. The aggregation may be minimized by a shorter reaction time, and the colloidal stabilization improved by increasing the concentration of stabilizer [87,88]. The fact that citrate also acts as reductant and pH-mediator in the synthesis makes is difficult to predict the effects of increased citrate concentration on Au NP morphology [88]. Furthermore, the insufficient colloidal stabilization of Au NPs at 140 °C may have originated from partial degradation of citrate. It has been shown that degradation of citrate occurs at higher temperature [89,90], but its thermal stability may be affected when applied as capping agent [90,91].

4.2.4 Scale-up of flow production

A common aim for Paper III and Paper IV was to investigate flow synthesis scalability, with the aim of targeting future applications. Flow reactors benefit from easy scalability, safe operation and sustainability. However, several scalability challenges exist which include maintaining NP uniformity and minimize fouling, and integration of inline monitoring of NP consistency. Scale-up of microfluidic flow reactors is achieved by operation of the reactor for longer time periods, by several reactors run in parallel, or the dimensions of the flow channels can be increased. The production of Pd NCs (Paper III) was first scaled up by setting up a micro-sized nucleation zone (inner diameter 800 μm) followed by connection to a milli-sized growth zone (inner diameter 1.4 mm). The larger volume of the reactor led to an 8-fold increase of the production rate. Nonetheless, the synthesis yield in this flow reactor decreased drastically compared to the micro-sized flow reactor (33 %) which could be due to the extensive fouling on the reactor walls. Interestingly, the Pd NCs synthesized in the milli-sized flow reactor have equivalent size and shape uniformity (14 nm $\pm$ 11 %) compared to the micro flow reactor. It should be noted that the particle size distribution was calculated from TEM-images which may not be representative of the quality of the whole batch. Furthermore, the second scale-up approach of Pd NCs and PdPt NP synthesis was by extension of the operation time of the micro-sized flow reactor (120 min). During the extended synthesis times, fouling occurred in the polymer tubing which led to more heterogeneous sized and shaped Pd NCs (Figure 4.11a) and PdPt NPs (Figure 4.11d).

The motivation to scale-up the synthesis of Pd NCs and PdPt NPs was the catalytic evaluation in a model NO_2 reduction reaction. During catalytic evaluation, the NP catalysts were exposed to reagents at elevated temperatures and the effect on the morphology is therefore studied (Figure 4.11).

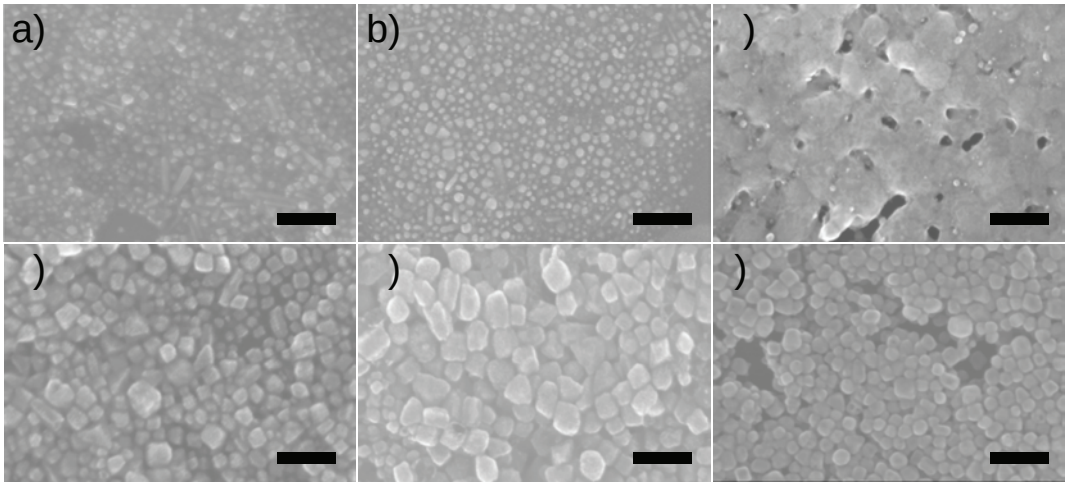

Figure 4.11: Structural characterization by SEM of Pd NCs (a,b and c) and PdPt NPs (d,e and f) synthesized in large-scale in the single-phase microsized flow reactor. NP samples were deposited on Si-substrates. a) Pd NCs and d) PdPt NPs without treatment. b) Pd NCs and e) PdPt NPs after treatment in 48-136 °C temperature interval. c) Pd NCs and f) PdPt NPs after treatment in 48-220°C temperature interval. Prior to heat treatments, pre-treatment was performed at 158 °C. Heat treatments were conducted in 2200 ppm NO_2 and 2.2 % H_2 in Ar(g). Scale bars are 100 nm.

After treatment in reaction conditions (48-136 °C), Pd NCs have slightly rounded edges (Figure 4.11b), and upon further temperature increase (220 °C), particles underwent sintering and formed large agglomerates(Figure 4.11c). The PdPt core-shell NPs on the other hand showed good thermal stability and retained the shapes at reaction conditions (Figure 4.11e), and the shape remained preserved at elevated temperatures (Figure 4.11f). The improved thermal stability experienced by the PdPt core-shell NPs may be attributed to the dendritic crystal structure, and the combination of Pd with Pt, which has a higher temperature stability [92]. The severe aggregation of the Pd NCs experienced at elevated temperatures (>220 °C), where the NPs lost their size and shape can be explained by sintering. Sintering can occur by two different mechanisms; Ostwald ripening, where small particles dissolve and redeposit onto large particles, or particle migration and coalescence[92, 93]. It is not fully understood by which mechanism sintering occurred for the Pd NPs, but a correlation between high NP concentration and sintering could be observed, where shorter inter-particle distance seemed to enhance the sintering process. It should also be pointed out that for this model catalytic reaction the NP catalysts were simply deposited on Si-substrates. Heterogeneous catalysis is normally performed with metal NP catalysts immobilized onto a porous support material. Several strategies have been employed to improve the sintering stability of metal NP catalysts to minimize diffusion, including enhancing metal-support interactions [94].

It would hence be interesting to re-evaluate the thermal stability of the NPs on mesoporous support materials. Moreover, it has been shown that highly monodisperse NPs experience less sintering due to Ostwald ripening effects [95]. Therefore, it would be very interesting to evaluate and compare the temperature stability of more shape- and size-uniform Pd NCs and PdPt NPs.

Fouling, which was experienced during scale-up in the flow reactors in Paper III, is a commonly encountered problem in single-phase flow reactors. Any interfaces can act as nucleation zones during NP growth, and since the reactants in single-phase flow reactors are in constant contact with the reactor wall there is high risk for heterogeneous nucleation and accelerated growth to occur on the reactor wall, which can lead to reactor fouling [45–47]. A possible solution is to use segmented flow reactors where the contact between the reactor wall and the reaction phase can be minimized by the use of an organic carrier phase that effectively wets the reactor walls. In the segmented flow synthesis of citrate-capped Au NPs no fouling was observed in the flow reactor, even when the synthesis was scaled-up for an extended time period (120 min). This indicates that the segmented flow effectively minimizes contact between the reaction phase and the reactor wall. It would be interesting to develop a fouling-free segmented flow synthesis of the Pd NCs and PdPt NPs that would enable an effective scale-up of the synthesis and that likely would produce more uniform NPs.

The segmented flow created large volumes of organic solvent waste (carrier phase). In Paper IV, a recycling strategy was implemented to separate Au NPs from the organic phase by using LLS, where the two phases efficiently can be separated based on polarity and the carrier phase recovered and reused in the synthesis. Au NPs after LLS show a zeta potential of -60 mV and maintain colloidal stabilization after separation of the reaction phase. Slight agglomeration could be observed when the Au NPs were placed onto TEM-grids, which could be an effect from drying the NP suspension or may originate from after the LLS.

An important part in continuous flow production scale-up is the monitoring of growth and NP product consistency using inline quality control [21, 46]. During the scale-up of the hydrothermal segmented flow synthesis of Au NPs, the product consistency was monitored inline using an UV-Vis spectroscopy flow cell during 54 min of synthesis (Figure 4.12). As can be seen in the contour plot (left Figure 4.12), the absorbance spectra of the Au NPs stay fairly consistent, as well as the absorbance maximum for each spectrum (marked with red diamonds) that presented an average peak maximum of 520.3 nm with a standard deviation of 2.8 nm (0.5 %). The representative inline UV-Vis spectrum of Au NPs (right Figure 4.12) correlates well with the ex-situ UV-Vis spectrum (Figure 4.9d). Some points in the contour plot show slightly lower

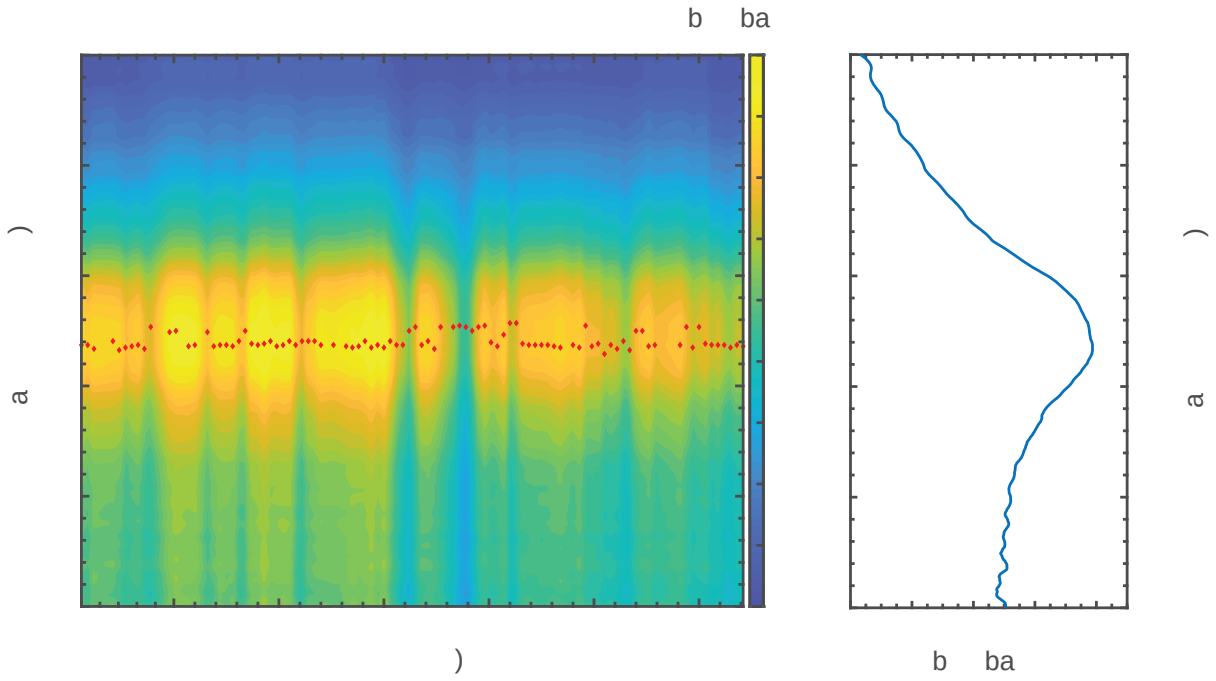

Figure 4.12: Left panel shows a contour plot which visualizes the inline UV-Vis absorption spectra of citrate-capped Au NPs recorded between 60-3120 seconds during continuous production. The absorbance maxima of each spectrum are marked with red diamonds. Right panel shows a representative inline UV-Vis spectrum of Au NPs.

absorbances and red-shift of the absorbance maxima, which may be due to slight agglomeration of Au NPs. It should be noted that the spectra were recorded during short integration time (1 ms) and the flow cell may be sensitive to external disturbances such as vibrations and air bubbles that may contribute to deviations in absorbance. Since the plasmon peaks are not very defined for Pd NCs and PdPt NPs, quality monitoring by inline UV-Vis spectroscopy is more challenging for these flow synthesized NPs.

When comparing the two systems developed to synthesize NPs in flow in larger scale there exist several important differences. The type of pumps used is important when it comes to scaling up the flow synthesis. In Paper III, a syringe pump was used to infuse the reagents. This type of pump is consequently limited by the volume of the syringes and can only produce a certain volume of NP suspension. In Paper IV, automated peristaltic pumps were used and the production volume was not as limited since bottled reagents were used for the precursor solutions. The advantage of the fouling-free segmented flow synthesis of citrate-capped Au NPs is that it was fully automated and integrated with inline quality control. The full automation provides lower maintenance and safer operation and this system demonstrates the capability of NP synthesis scale-up for future real applications like the catalysis of NO_2 reduction, as explored for a test reaction in the following section.

4.2.5 Catalytic evaluation of Pd and PdPt nanoparticles

In Paper III, a coauthor performed a temperature programmed NO_2 reduction reaction (48-136 °C with a gas feed of 2200 ppm NO_2 and 2.2 % H_2 in argon) using a flow "pocket reactor" to study the catalytic activity of Pd NCs and PdPt core-shell NPs. The corresponding NO_2 conversion efficiencies (Figure 4.13a) show that PdPt core-shell NPs exhibited slightly higher catalytic activity at lower temperatures. The lower activity of Pd NCs could partly be related to the cubic structure, which is composed of (100) crystal facets, known to exhibit lower activity compared to high-index facet counterparts[96–99] that are highly abundant in the dendritic PdPt NPs. Additionally, synergistic effects between Pd and Pt may have contributed to the improved catalytic activity of PdPt NPs. Product selectivity is another aspect studied. During NO_2 reduction by H_2 three products form; NO, N_2O, and N_2, where N_2 is the most desired one due to its non-toxicity compared to the others, which are greenhouse gases and/or toxic. There is a clear difference in selectivity between the two types of NPs (Figure 4.13b), where the PdPt core-shell NPs show higher selectivity towards N_2, as well as lower selectivity for NO formation compared to the Pd NCs who show nearly 98 % NO selectivity. It should be noted that due to restructuring behavior that was observed for the NPs at elevated temperatures, the operation temperature was limited to 150 °C. An improved temperature stability would enable the temperature window to be extended, likely resulting in lower NO selectivity. Moreover, since the synthesis scale-up produced heterogeneous NPs it would be interesting for future studies to evaluate the catalytic activity and selectivity of uniform shaped NPs, which would deepen the understanding of the relationship between catalytic performance and shape.

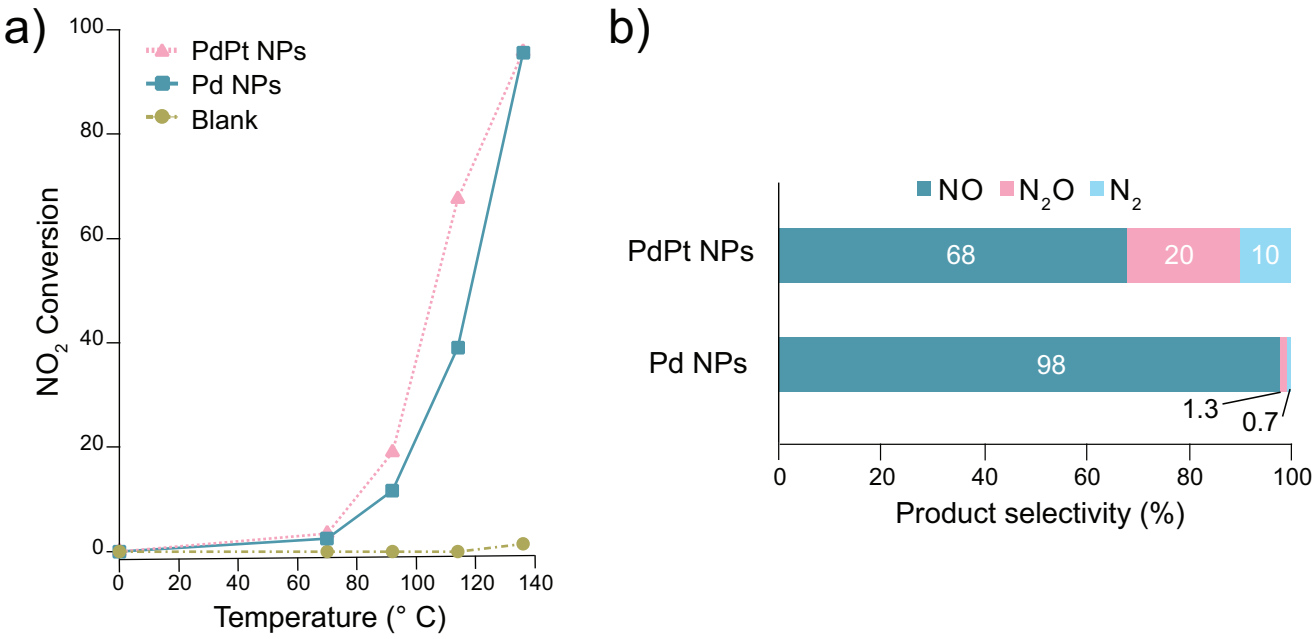

Figure 4.13: Catalytic evaluation of Pd NCs and PdPt NPs. a) Relative NO_2 conversion efficiencies of Pd NCs, PdPt NPs and blank sample. b) Calculated relative percent selectivity of NO, N_2O and N_2 in 48 – 136 °C temperature interval for Pd NCs and PdPt NPs. Adapted with permission from Ref. [81]. Copyright (2019) American Chemical Society.

Chapter 5

Conclusions and Reflections

The aim of the work presented in this thesis was to improve the understanding of the factors that control the synthesis of shape and size-controlled metal NPs using solution-based colloidal methods. From the studies presented in the first part of this thesis, it can be concluded that the stabilizers strongly influence the NP properties which include stability, shape and reduction kinetics. I found that the selected stabilizers can have more roles than providing colloidal stabilization. Thiolate stabilizers decompose at the surface of Cu NPs and only provide temporary stabilization of the NP surface, even under inert atmosphere. In the synthesis of Pd NPs in the absence of traditional reductants, it can be concluded that the fatty acid stabilizers NaOL and NaST contribute to the reduction of Pd-precursors. Quantitative evaluation of the reduction kinetics show that these stabilizers exhibit pseudo first-order reduction kinetics in the synthesis of Pd NPs, where the unsaturated fatty acid NaOL provides faster and more effective reduction. The different stabilizers' influence on reduction kinetics direct the sizes and shapes of the Pd NPs.

The second part presented in this thesis focused on the development of flow synthesis routes for the design of shaped and uniform metal NPs, and provided synthesis scalability and catalytic evaluation. First, I developed a single-phase flow reactor that produced shape- and size-controlled Pd NCs and PdPt NPs. Precise morphological control of core-shell PdPt NPs was achieved by varying the elemental composition. Secondly, a fouling-free segmented flow synthesis was developed to produce uniform Au NPs. In both syntheses, among the evaluated reaction parameters temperature strongly influenced NP properties. Synthesis scale-up in the single-phase reactor led to extensive fouling and heterogeneous NPs. Exposure of these NPs to elevated temperatures showed that the bimetallic PdPt NPs exhibit better stability compared to the monometallic Pd NCs. Furthermore, from a proof-of-concept catalytic evaluation in the NO_2 reduction reaction it can be concluded that PdPt NPs also exhibit higher catalytic activity and

improved product selectivity. The scale-up of the segmented flow system provided uniform Au NPs and the product consistency was confirmed by inline optical spectroscopy. The fully automated and segmented flow system thus presents a promising system for scalable synthesis of precisely controlled NPs.

5.1 Contribution to the field of nanoparticle synthesis

I gained several insights from the studies presented in this thesis. I hope these findings will contribute to the further development within the research field of NP synthesis. Firstly, it is well-known that stabilizers can have multiple roles in the synthesis of metal NPs. I have gained an improved understanding of the roles of some stabilizers applied in the synthesis of metal NPs, how the stabilizers can direct the NP stability, shape and reduction kinetics. I am convinced that these studies can contribute to better knowledge on how these specific stabilizers interact and influence NP properties. Secondly, the different flow synthesis routes presented in this thesis will possibly serve as examples and inspiration for further refinements and development of new flow techniques for the production of controlled metal NPs. The process scalability of the two flow methods was demonstrated for the production of NPs. Nonetheless, the production scales evaluated in these studies are still in the milligram to gram scale. Additional work is needed to further refine and develop the methods to target kilogram scale production capacity required for real industrial applications. Several approaches can be explored to reach this goal such as operating several reactors in parallel, incorporating in-situ quality control and automated feedback loops. These are some of the aspects that I will discuss in the next section.

5.2 Reflections on future development of nanoparticle synthesis

The future of metal NP synthesis holds exciting opportunities, where automation and intelligent synthesis are interesting areas for exploration. In the coming years, NP synthesis development will likely expand from traditional trial-and-error approaches and include intelligent synthesis optimization, using artificial intelligence (AI) and machine learning [21, 100–102]. Fully automated segmented flow systems are promising platforms for this development. Instead of replacing experimentalists, I believe these new tools will strengthen and speed up the NP development processes. From the studies presented in this thesis I found that some stabilizing molecules can act as reductants in the synthesis, and further research into these capabilities might expand the flow synthesis but only if we understand how these reductants are functioning. This may require

a combination of automated flow synthesis and machine learning to change reaction conditions quickly, and experimentalists to choose the most likely factors to test.

Furthermore, NP synthesis should take inspiration from flow synthesis of organic compounds, which in recent years have seen developments in automated synthesis using AI in planning and screening of reaction conditions to predict optimal reaction conditions [103]. This can also be applied to NP synthesis, where machine learning can serve as a powerful tool for synthesis optimization by the use of automated feedback loops. By bringing knowledge from existing NP synthesis data, reaction parameter space optimization can be performed to estimate and optimize NP outcomes [49, 104, 105]. Fully automated segmented flow systems with in-situ monitoring coupled to machine learning and optimization algorithms may enable effective reaction monitoring and NP synthesis optimization. Altogether, I believe these future technological developments could facilitate production scale-up for real industrial applications and may shorten the time for new high-performing controlled NPs to reach industrial applications.

Acknowledgements

These PhD studies have been a journey for me, both professionally and personally, and has involved deep valleys and important life lessons learned over these four years. I want to thank all the people who have been involved in this process to support me to finally reach this big goal.

My second supervisor Prof. Kasper Moth-Poulsen for giving me the opportunity to start this PhD project. For all your scientific inputs and guidance, and I am glad to have experienced how our relationship has developed over the years.

My main supervisor Prof. Hanna Härelind for your strong support and supervision and guidance. You helped me believe in myself, all the way to the PhD. Thanks for all the amazing times together during research projects, and outside work at the division parties.

My examiner Prof. Martin Andersson. You sparked my interest in research when you took me in as a master thesis student in 2014, which eventually led me to start this journey. Thank you for your scientific support and guidance during this time.

Prof. Victor Sebastian for hosting me during my research stay in University of Zaragoza in Spain. I am grateful for your supervision in developing flow chemistry methods and the personal developments I experienced during this research stay.

The Flow team: Jessica and Robson. Thanks for great times together in the lab, with lots of laughter, interesting scientific discussions and achievements.

My friends and colleagues at the division of applied chemistry. Thank you for amazing times together with fikas, parties, trips, and good times in the lab. No one mentioned, no one forgotten.

My dear friends, who mean so much to me. You have been by my side all this time. You know who you are. Thank you all for your support.

Ett speciellt tack till min familj. Ni har stöttat mig och alltid funnits där för mig i de bra och de svåra stunderna. Jag är väldigt tacksam för det. Jag älskar er.

Älskade Carl-Robert, min klippa. De snart två år som du har varit en del av mitt liv har varit fantastiska. Du har funnits där och har stöttat mig varje dag i att kämpa på och fortsätta. Jag ser nu fram emot att fortsätta vår resa tillsammans mot en spännande framtid. Jag älskar dig.

Bibliography

[1] T. S. Rodrigues, A. G. Da Silva, and P. H. Camargo, *Journal of Materials Chemistry A*, 2019, **7**(11), 5857–5874.

[2] H. Lee, *RSC Advances*, 2014, **4**(77), 41017–41027.

[3] S. Guo and E. Wang, *Nano Today*, 2011, **6**(3), 240–264.

[4] S. Zeng, K. T. Yong, I. Roy, X. Q. Dinh, X. Yu, and F. Luan, *Plasmonics*, 2011, **6**(3), 491–506.

[5] L. Dykman and N. Khlebtsov, *Chemical Society Reviews*, 2012, **41**(6), 2256–2282.

[6] Z. Fan and H. Zhang, *Chemical Society Reviews*, 2016, **45**(1), 63–82.

[7] J. Pal and T. Pal, *Nanoscale*, 2015, **7**(34), 14159–14190.

[8] L. Zhang and Y. Xia, *Advanced Materials*, 2014, **26**(16), 2600–2606.

[9] T. K. Sau and A. L. Rogach, *Advanced Materials*, 2010, **22**(16), 1781–1804.

[10] H. You, S. Yang, B. Ding, and H. Yang, *Chemical Society Reviews*, 2013, **42**(7), 2880–2904.

[11] S. Cheong, J. D. Watt, and R. D. Tilley, *Nanoscale*, 2010, **2**(10), 2045–2053.

[12] T. H. Yang, K. D. Gilroy, and Y. Xia, *Chemical Science*, 2017, **8**(10), 6730–6749.

[13] S. E. Lohse, J. R. Eller, S. T. Sivapalan, M. R. Plews, and C. J. Murphy, *ACS Nano*, 2013, **7**(5), 4135–4150.

[14] J. S. Santana and S. E. Skrabalak, *Advanced Energy Materials*, 2019, **1902051**, 1–14.

[15] E. J. Roberts, L. R. Karadaghi, L. Wang, N. Malmstadt, and R. L. Brutchey, *ACS Applied Materials & Interfaces*, 2019, **11**(31), 27479–27502.

[16] P. R. Makgwane and S. S. Ray, *Journal of Nanoscience and Nanotechnology*, 2014, **14**(2), 1338–1363.

[17] R. M. Myers, D. E. Fitzpatrick, R. M. Turner, and S. V. Ley, *Chemistry - A European Journal*, 2014, **20**(39), 12348–12366.

[18] G. Niu, A. Ruditskiy, M. Vara, and Y. Xia, *Chem. Soc. Rev.*, 2015, **44**(16), 5806–5820.

[19] C. T. Riche, E. J. Roberts, M. Gupta, R. L. Brutchey, and N. Malmstadt, *Nature Communications*, 2016, **7**, 1–7.

[20] L. Zhang, G. Niu, N. Lu, J. Wang, L. Tong, L. Wang, M. J. Kim, and Y. Xia, *Nano Letters*, 2014, **14**(11), 6626–6631.

[21] L.-J. Pan, J.-W. Tu, H.-T. Ma, Y.-J. Yang, Z.-Q. Tian, D.-W. Pang, and Z.-L. Zhang, *Lab on a Chip*, 2017, **18**, 41–56.

[22] T. S. Rodrigues, M. Zhao, T. H. Yang, K. D. Gilroy, A. G. da Silva, P. H. Camargo, and Y. Xia, *Chemistry - A European Journal*, 2018, **24**(64), 16944–16963.

[23] A. Heuer-Jungemann, N. Feliu, I. Bakaimi, M. Hamaly, A. Alkilany, I. Chakraborty, A. Masood, M. F. Casula, A. Kostopoulou, E. Oh, K. Susumu, M. H. Stewart, I. L. Medintz, E. Stratakis, W. J. Parak, and A. G. Kanaras, *Chemical Reviews*, 2019, **119**(8), 4819–4880.

[24] V. K. Lamer and R. H. Dinegar, *Journal of the American Chemical Society*, 1950, **72**(11), 4847–4854.

[25] Z. Wu, S. Yang, and W. Wu, *Nanoscale*, 2016, **8**(3), 1237–1259.

[26] M. Muzzio, J. Li, Z. Yin, I. M. Delahunty, J. Xie, and S. Sun, *Nanoscale*, 2019, **11**(41), 18946–18967.

[27] Y. Xia, X. Xia, and H. C. Peng, *Journal of the American Chemical Society*, 2015, **137**(25), 7947–7966.

[28] N. T. K. Thanh, N. Maclean, and S. Mahiddine, *Chemical Reviews*, 2014, **114**(15), 7610–7630.

[29] J. Polte, *CrystEngComm*, 2015, **17**(5).

[30] T. H. Yang, Y. Shi, A. Janssen, and Y. Xia, *Angewandte Chemie - International Edition*, 2020, **59**(36), 15378–15401.

[31] L. D. Marks and L. Peng, *Journal of Physics Condensed Matter*, 2016, **28**(5), 53001.

[32] J. Gu, Y. W. Zhang, and F. Tao, *Chemical Society Reviews*, 2012, **41**(24), 8050–8065.

[33] A. Zaleska-Medynska, M. Marchelek, M. Diak, and E. Grabowska, *Advances in Colloid and Interface Science*, 2016, **229**, 80–107.

[34] M. B. Gawande, A. Goswami, T. Asefa, H. Guo, A. V. Biradar, D.-l. Peng, R. Zboril, and R. S. Varma, *Chemical Society Reviews*, 2015, **44**(21), 7540–7590.

[35] K. D. Gilroy, A. Ruditskiy, H. C. Peng, D. Qin, and Y. Xia, *Chemical Reviews*, 2016, **116**(18), 10414–10472.

[36] H. L. Liu, F. Nosheen, and X. Wang, *Chemical Society Reviews*, 2015, **44**(10), 3056–3078.

[37] M. Zhou, H. Wang, M. Vara, Z. D. Hood, M. Luo, T. H. Yang, S. Bao, M. Chi,

P. Xiao, Y. Zhang, and Y. Xia, *Journal of the American Chemical Society*, 2016, **138**(37), 12263–12270.

[38] J. Zhang, L. Wan, L. Liu, Y. Deng, C. Zhong, and W. Hu, *Nanoscale*, 2016, **8**(7), 3962–3972.

[39] X. Huang, Y. Li, Y. Li, H. Zhou, X. Duan, and Y. Huang, *Nano Letters*, 2012, **12**(8), 4265–4270.

[40] X. Xia, Y. Wang, A. Ruditskiy, and Y. Xia, *Advanced Materials*, 2013, **25**(44), 6313–6332.

[41] J. S. Santana, K. M. Koczkur, and S. E. Skrabalak, *Langmuir*, 2017, **33**(24), 6054–6061.

[42] E. Shahbazali, V. Hessel, T. Noël, and Q. Wang, *Nanotechnology Reviews*, 2014, **3**(1), 65–86.

[43] S. Marre and K. F. Jensen, *Chemical Society reviews*, 2010, **39**(3), 1183–1202.

[44] S. E. Lohse, *Physical Sciences Reviews*, 2018, **3**(11), 1–29.

[45] J. M. Köhler, S. Li, and A. Knauer, *Chemical Engineering and Technology*, 2013, **36**(6), 887–899.

[46] H. Huang, H. du Toit, L. Panariello, L. Mazzei, and A. Gavriilidis, *Physical Sciences Reviews*, 2018, **3**, 157–220.

[47] Y. He, K. J. Kim, and C. H. Chang, *Nanomaterials*, 2020, **10**(7), 1–21.

[48] Y. Shen, N. Weeranoppanant, L. Xie, Y. Chen, M. R. Lusardi, J. Imbrogno, M. G. Bawendi, and K. F. Jensen, *Nanoscale*, 2017, **9**(23), 7703–7707.

[49] V. Sebastian, S. A. Khan, and A. A. Kulkarni, *Journal of Flow Chemistry*, 2017, **7**(3–4), 96–105.

[50] K. Pacławski, B. Streszewski, W. Jaworski, M. Luty-Błocho, and K. Fitzner, *Colloids and Surfaces A: Physicochemical and Engineering Aspects*, 2012, **413**, 208–215.

[51] L. C. McKenzie, P. M. Haben, S. D. Kevan, and J. E. Hutchison, *Journal of Physical Chemistry C*, 2010, **114**(50), 22055–22063.

[52] V. Sebastian Cabeza, S. Kuhn, A. a. Kulkarni, and K. F. Jensen, *Langmuir*, 2012, **28**(17), 7007–7013.

[53] G. Liu, X. Yang, Y. Li, Z. Yang, W. Hong, and J. F. Liu, *Advances in Materials Science and Engineering*, 2015, **2015**.

[54] J. W. Park, Z. Hu, S. Gao, I. H. Campbell, and H. Gong, *Geochimica et Cosmochimica Acta*, 2012, **93**, 63–76.

[55] H. Zhang, M. Jin, and Y. Xia, *Chemical Society Reviews*, 2012, **41**(24), 8035.

[56] C. Rohner, A. Pekkari, H. Härelind, and K. Moth-Poulsen, *Langmuir*, 2017, **33**(46).

[57] W. Niu, Z. Y. Li, L. Shi, X. Liu, H. Li, S. Han, J. Chen, and G. Xu, *Crystal Growth and Design*, 2008, **8**(12), 4440–4444.

[58] F. Kettemann, A. Birnbaum, S. Witte, M. Wuithschick, N. Pinna, R. Kraehnert, K. Rademann, and J. Polte, *Chemistry of Materials*, 2016, **28**(11), 4072–4081.

[59] D. B. Williams and C. B. Carter, *Transmission Electron Microscopy*, Springer, 2009.

[60] J. I. Goldstein, D. E. Newbury, J. R. Michael, N. W. M. Ritchie, J. H. J. Scott, and D. C. Joy, *Scanning Electron Microscopy and X-Ray Microanalysis*, Springer, 4 ed., 2018.

[61] C. J. le Roux and R. J. Kriek, *Hydrometallurgy*, 2017, **169**, 447–455.

[62] U. Kreibig and M. Vollmer, *Optical properties of metal clusters*, Springer, Berlin-New York, 1995.

[63] C. Suryanarayana and M. G. Norton, in *X-Ray Diffraction: A Practical Approach*, Springer US, Boston, MA, 1998; pp. 21–62.

[64] G. Moore in *Introduction to Inductively Coupled Plasma Atomic Emission Spectrometry*, ed. G. Moore, Analytical Spectroscopy Library; Elsevier, Amsterdam, 1989; pp. 65 – 90.

[65] P. R. Griffiths and J. A. de Haseth, *Fourier Transform Infrared Spectrometry*, John Wiley & Sons, 2 ed., 2007.

[66] H. Günther, *NMR Spectroscopy : Basic Principles, Concepts and Applications in Chemistry.*, John Wiley & Sons, Incorporated, 2013.

[67] S. Bhattacharjee, *Journal of Controlled Release*, 2016, **235**, 337–351.

[68] Y. Bu, J. W. Niemantsverdriet, and H. O. Fredriksson, *ACS Catalysis*, 2016, **6**(5), 2867–2876.

[69] M. D. Susman, A. Vaskevich, and I. Rubinstein, *Journal of Physical Chemistry C*, 2016, **120**(29), 16140–16152.

[70] S. Vollmer, G. Witte, and C. Wöll, *Langmuir*, 2001, **17**(24), 7560–7565.

[71] X. Ye, Y. Gao, J. Chen, D. C. Reifsnyder, C. Zheng, and C. B. Murray, *Nano Letters*, 2013, **13**(5), 2163–2171.

[72] H. C. Peng, S. Xie, J. Park, X. Xia, and Y. Xia, *Journal of the American Chemical Society*, 2013, **135**(10), 3780–3783.

[73] Y. H. Chen, H. H. Hung, and M. H. Huang, *Journal of the American Chemical Society*, 2009, **131**(25), 9114–9121.

[74] S. K. Meena, S. Celiksoy, P. Schäfer, A. Henkel, C. Sönnichsen, and M. Sulpizi, *Physical Chemistry Chemical Physics*, 2016, **18**(19), 13246–13254.

[75] M. A. Watzky and R. G. Finke, *Journal of the American Chemical Society*, 1997, **119**(43), 10382–10400.

[76] S. Özkar and R. G. Finke, *Langmuir*, 2016, **32**(15), 3699–3716.

[77] S. Mozaffari, W. Li, C. Thompson, S. Ivanov, S. Seifert, B. Lee, L. Kovarik, and A. M. Karim, *Nanoscale*, 2017, **9**(36), 13772–13785.

[78] M. Luty-Błocho, K. Pacławski, M. Wojnicki, and K. Fitzner, *Inorganica Chimica Acta*, 2013, **395**, 189–196.

[79] K. Raghunathan, J. Antony, S. Munir, J.-P. Andreassen, and S. Bandyopadhyay, *Nanoscale Advances*, 2020, **2**, 1980–1992.

[80] F. N. Stappen, K. Enemark-Rasmussen, G. P. Junor, M. H. Clausen, J. Zhang, and C. Engelbrekt, *Journal of Physical Chemistry C*, 2019, **123**(41), 25402–25411.

[81] A. Pekkari, Z. Say, A. Susarrey-Arce, C. Langhammer, H. Härelind, V. Sebastian, and K. Moth-Poulsen, *ACS Applied Materials and Interfaces*, 2019, **11**(39), 36196–36204.

[82] Y. Kim, Y. W. Lee, M. Kim, and S. W. Han, *Chemistry - A European Journal*, 2014, **20**(26), 7901–7905.

[83] A. Abou-Hassan, O. Sandre, and V. Cabuil, *Angewandte Chemie - International Edition*, 2010, **49**(36), 6268–6286.

[84] A. A. Kulkarni and V. Sebastian Cabeza, *Langmuir*, 2017, **33**(50), 14315–14324.

[85] J. Ftouni, M. Penhoat, A. Addad, E. Payen, C. Rolando, and J. S. Girardon, *Nanoscale*, 2012, **4**(15), 4450–4454.

[86] Y. Wang, H. C. Peng, J. Liu, C. Z. Huang, and Y. Xia, *Nano Letters*, 2015, **15**(2), 1445–1450.

[87] W. Ding, P. Zhang, Y. Li, H. Xia, D. Wang, and X. Tao, *ChemPhysChem*, 2015, **16**(2), 447–454.

[88] M. Wuithschick, A. Birnbaum, S. Witte, M. Sztucki, U. Vainio, N. Pinna, K. Rademann, F. Emmerling, R. Kraehnert, and J. Polte, *ACS Nano*, 2015, **9**(7), 7052–7071.

[89] A. Marcilla, A. Gómez-Siurana, M. Beltrán, I. Martínez-Castellanos, I. Blasco, and D. Berenguer, *Journal of the Science of Food and Agriculture*, 2018, **98**(15), 5916–5931.

[90] Z. Bai, L. Yang, J. Zhang, L. Li, C. Hu, J. Lv, and Y. Guo, *Journal of Power Sources*, 2010, **195**(9), 2653–2658.

[91] M. Bajaj, N. Wangoo, D. V. Jain, and R. K. Sharma, *Scientific Reports*, 2020, **10**(1), 1–7.

[92] A. Cao, R. Lu, and G. Veser, *Physical Chemistry Chemical Physics*, 2010, **12**(41), 13499–13510.

[93] T. W. Hansen, A. T. Delariva, S. R. Challa, and A. K. Datye, *Accounts of Chemical Research*, 2013, **46**(8), 1720–1730.

[94] L. Wang, L. Wang, X. Meng, and F. S. Xiao, *Advanced Materials*, 2019, **31**(50),

1–18.

[95] V. P. Zhdanov, E. M. Larsson, and C. Langhammer, *Chemical Physics Letters*, 2012, **533**, 65–69.

[96] D. L. Feldheim, *Science*, 2007, **316**(5825), 399–700.

[97] N. Tian, Z. Y. Zhou, N. F. Yu, L. Y. Wang, and S. G. Sun, *Journal of the American Chemical Society*, 2010, **132**(22), 7580–7581.

[98] B. Y. Xia, H. B. Wu, X. Wang, and X. W. Lou, *Angewandte Chemie - International Edition*, 2013, **52**(47), 12337–12340.

[99] E. Ozensoy, C. Hess, and D. W. Goodman, *Journal of the American Chemical Society*, 2002, **124**(29), 8524–8525.

[100] B. J. Reizman and K. F. Jensen, *Accounts of Chemical Research*, 2016, **49**(9), 1786–1796.

[101] J. Nette, P. D. Howes, and A. J. DeMello, *Advanced Materials Technologies*, 2020, **5**(7).

[102] R. M. Maceiczyk, I. G. Lignos, and A. J. Demello, *Current Opinion in Chemical Engineering*, 2015, **8**, 29–35.

[103] C. W. Coley, D. A. Thomas, J. A. M. Lummiss, J. N. Jaworski, C. P. Breen, V. Schultz, T. Hart, J. S. Fishman, L. Rogers, H. Gao, R. W. Hicklin, P. P. Plehiers, J. Byington, J. S. Piotti, W. H. Green, A. J. Hart, T. F. Jamison, and K. F. Jensen, *Science*, 2019, **365**(6453), 1–9.

[104] O. Voznyy, L. Levina, J. Z. Fan, M. Askerka, A. Jain, M. J. Choi, O. Ouellette, P. Todorović, L. K. Sagar, and E. H. Sargent, *ACS Nano*, 2019, **13**(10), 11122–11128.

[105] A. M. Hiszpanski, B. Gallagher, K. Chellappan, P. Li, S. Liu, H. Kim, J. Han, B. Kailkhura, D. J. Buttler, and T. Y. J. Han, *Journal of Chemical Information and Modeling*, 2020, **60**(6), 2876–2887.